

Coherent Light Shift on Alkaline-Earth Rydberg Atoms from Isolated Core Excitation without Autoionization

Ky-Luc Pham¹, Thomas F. Gallagher^{2,*}, Pierre Pillet¹, Steven Lepoutre¹, and Patrick Cheinet^{1,†}

¹Université Paris-Saclay, CNRS, Laboratoire Aimé Cotton, 91405 Orsay, France

²Department of Physics, University of Virginia, Charlottesville, Virginia 22904, USA

 (Received 1 November 2021; revised 15 February 2022; accepted 24 March 2022; published 6 May 2022)

New experimental quantum simulation platforms have recently been implemented with divalent atoms trapped in optical tweezer arrays, with promising performance. The second valence electron also brings about new prospects through the so-called isolated core excitation (ICE). However, autoionization presents a strong limitation to this use. In this study, we propose and demonstrate a new approach to applying a sizable light shift to a Rydberg state with close-to-resonant ICE while avoiding autoionization. In particular, we investigate the ICE of ytterbium atoms in 1S_0 Rydberg states. Spectroscopic studies of the induced autoionization and the light shift imparted to the Rydberg states are well accounted for with multichannel quantum defect theory. Such control over the inner electron without disturbing the Rydberg electron brings about a new tool for the targeted coherent manipulation of Rydberg states in quantum simulation or quantum computing experiments performed with alkaline-earth atoms.

DOI: [10.1103/PRXQuantum.3.020327](https://doi.org/10.1103/PRXQuantum.3.020327)

I. INTRODUCTION

Quantum simulation is an appealing prospect offered by experiments based on cold neutral atoms and Rydberg excitations [1] constitute an efficient tool to perform quantum operations [2–5], providing strong interactions between electric dipoles [6,7]. Experimental confirmation of these assets has first been evidenced in quantum gas microscopes [8–11]. Building on this progress, new platforms based on Rydberg excitations of alkali atoms trapped in arrays of optical tweezers have been designed to engineer strongly correlated many-body ensembles [12–14]. Groundbreaking experiments have been reported with these platforms in the domains of quantum simulation [15–21] and its digital counterpart, quantum computing [22–24], demonstrating the relevance of this approach for quantum information processing.

Within this framework, proof-of-principle experiments have demonstrated the interest in addressing specific sites with focused laser beams, in order to create a localized Rydberg excitation [23] or to shift an atomic level [22,24–26]. In this respect, monovalent alkali atoms

present the drawback that the techniques to manipulate—cool, image, or light shift—ground-state atoms are inefficient when applied to Rydberg states. Several workarounds have been found for indirect imaging [8,27], specific targeting of a lower energy level [28,29], or trapping in the repulsive ponderomotive potential seen by the Rydberg electron [30–34] but their experimental application is demanding. Overall, this lack of control over Rydberg states has potentially detrimental effects on the performance of quantum operations, because Rydberg states are ejected by the tweezer light [12,22,35], whereas a shift of the ground state alters the tweezer potential [25].

Recently, attention has been drawn to the opportunities offered by alkaline-earth species [36]. The presence of a second valence electron provides a rich internal structure with attractive properties for quantum simulation [37,38] and quantum computing [39,40]. This structure also offers efficient laser cooling [41], leading to very effective simultaneous cooling and imaging in quantum gas microscopes [42] and optical tweezers [43–46]. It has led to a proof-of-principle demonstration of quantum operations with alkaline-earth atoms, with outstanding performance [47].

Interest is not confined to low-lying states of alkaline-earth atoms but extends to their Rydberg states [36,48]. A promising resource of divalent species resides in the isolated core excitation (ICE) of a Rydberg state, which consists of driving an optical transition of the remaining valence core electron with the Rydberg electron remaining a spectator [49]. However, a severe limitation in the application of ICE is the autoionization (AI) of a Rydberg state

*tfg@virginia.edu

†patrick.cheinet@u-psud.fr

Published by the American Physical Society under the terms of the [Creative Commons Attribution 4.0 International license](https://creativecommons.org/licenses/by/4.0/). Further distribution of this work must maintain attribution to the author(s) and the published article's title, journal citation, and DOI.

with an excited core [49]. In this process, the electrostatic interaction between Rydberg and core electrons leads to the simultaneous ejection of one electron and relaxation of the other to a lower-energy state. While AI can be an asset as a diagnostic tool, as demonstrated with strontium [50–53], it represents a major obstacle for the coherent, or at least lossless, manipulation of Rydberg states.

The consideration of ICE far from resonance may allow its use as a trap [48,54] but residual losses are still constrained by AI rates that are usually much larger than radiative decay rates. Moreover, far off-resonant traps demand high laser power and do not address Rydberg states selectively, contrary to near-resonant ICE. Another approach is to consider Rydberg states with high angular momentum ℓ , which are known to exhibit low AI rates when their core is excited [55–57]. Indeed, the Rydberg electron never comes near the core, resulting in AI rates that can become smaller than the radiative decay rate of the excited ion core. The use of high- ℓ Rydberg states, possibly up to the circular states [58], thus allows familiar approaches to cooling, imaging, and the production of coherent energy shifts but at the price of substantially increased experimental complexity.

Here, we introduce a near-resonant ICE approach that allows large light shifts of low-angular-momentum Rydberg states while suppressing AI. It is based on the existence of minima occurring in the ICE photoexcitation rate, previously observed with atomic beams [49,59,60], called autoionization zeros (AIZs). In the following, we start by outlining the essential ideas of ICE, introduce an efficient treatment of its effects using the multichannel quantum defect theory (MQDT), and discuss its physical predictions, in order to prepare a synthetic presentation of our experimental results. We then describe measurements of ICE photoexcitation spectra of $6sn_s\ ^1S_0$ Rydberg states of ytterbium (Yb) that confirm the existence of AIZs. Subsequently, we use Rydberg-excitation spectroscopy to measure the spectral shift induced by ICE and verify the existence of a sizable shift at the AIZ. Finally, we comment on new applications in quantum simulation or quantum computing offered by this technique. While preparing this paper, we have become aware of a similar study with $6sns\ ^3S_1$ states of Yb that has also uncovered useful AIZs [61].

II. ICE AND MQDT

A. Basic concepts

We start by presenting the simplest configuration possible for the near-resonant ICE applied to a divalent atom in a Rydberg state and introduce the relevant parameters. More complicated configurations might require the addition of supplementary channels for a precise evaluation of the effects of ICE, as discussed in Sec. VI. However, despite the notation chosen for application to Yb, the

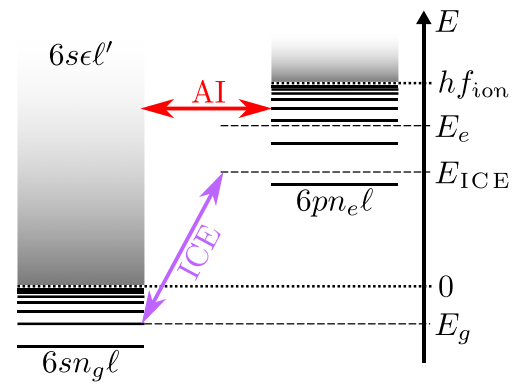


FIG. 1. The energy-level diagram (not to scale) for the MQDT treatment of ICE with two channels. The purple arrow represents an ICE photon connecting the initial state in the $6sn_g\ell$ Rydberg series with a ground-state core to a Rydberg series $6pn_e\ell$ with an excited core. The red horizontal arrow shows AI as a coupling between this doubly excited series and the continuum state $6s\epsilon\ell'$, where ϵ is the kinetic energy of the ejected electron. The energy scale on the right introduces the energy levels (dashed, horizontal lines) used in the MQDT treatment. The two Rydberg-series ionization limits are represented using horizontal dotted lines. With the first taken as energy reference, the second has an energy hf_{ion} .

approach presented provides the essential analysis for most experiments involving ICE.

We consider an atom initially prepared in a bound Rydberg state with a ground-state core, denoted by $6sn_g\ell$, of energy E_g (Fig. 1): $6s$ describes the core-electron state, n_g is the principal quantum number of the Rydberg electron, and ℓ is its orbital-angular-momentum quantum number. This Rydberg series converges ($n_g \rightarrow \infty$) to the first ionization limit set at energy $E = 0$. The atom is illuminated by ICE light with frequency f_{ICE} close to resonance with an optical transition of the ionic core, addressing the energy $E_{ICE} = E_g + hf_{ICE}$. The ICE hypothesis assumes that the ICE light acts only on the core electron, while the Rydberg electron remains a spectator: near-resonant ICE thus couples the $6sn_g\ell$ state with doubly excited Rydberg states belonging to the series $6pn_e\ell$ with the core electron excited in the $6p$ level and $n_e \sim n_g$. This series converges to another ionization limit at the energy hf_{ion} , corresponding to the energy of the $6s \leftrightarrow 6p$ ion transition. Atoms excited within this series may autoionize due to a coupling to the continuum state $6s\epsilon\ell'$, where ϵ is the kinetic energy of the ejected electron. It results in a quasicontinuum and its energy is denoted by E_e . In general, the AI rate is much greater than the spontaneous emission rate of the ion in state $6p$, which is assumed to be negligible in our experimental conditions. Therefore, detection of an ionized state is the signature of photoexcitation of the initial state toward a $6pn_e\ell$ state, always followed by AI. Here and in the following, we consider the effects of ICE only from the viewpoint of the $6sn_g\ell$ state. Therefore, we term as “AI of the $6sn_g\ell$ state” the full process consisting in

photoexcitation followed by AI. In particular, the term ‘‘AI rate’’ is now used instead of photoexcitation rate (the same goes for the cross section) and ICE photoexcitation spectra are referred to as AI spectra.

Qualitatively, when $n_e = n_g$, the coupling to the continuum induces a Lorentzian broadening around the $6s n_g \ell$ - $6p n_e \ell$ resonance, with an amplitude inversely proportional to its width, spreading the $6s \leftrightarrow 6p$ oscillator strength over the AI width. This width is proportional to the Rydberg-electron density distribution close to the core, scaling as $1/n^3$. Thus the peak AI cross section is expected to scale as n^3 . While the AI cross section is Lorentzian near its peak, it is not in the far wings, because the $6p n_e \ell$ state is not an isolated state but a member of a Rydberg series. In Sec. II B, we use MQDT to treat this multiple-state problem. It converts the simple physical picture of the ICE hypothesis into a quantitative expression for the ICE spectrum and the energy shift of the bound $6s n_g \ell$ state imparted by ICE light.

B. Two-channel MQDT model

In this section, we define the relevant quantities and introduce the general principles of the MQDT treatment, which is detailed in Appendix A. It results in unified formulas that simplify the presentation of our measurements.

We consider two physical effects of ICE on the Rydberg atom in a $6s n_g \ell$ state: its AI and the appearance of a conservative potential denoted as an energy shift $(\Delta E)_{\text{ICE}}$. AI proceeds with a rate Γ that is proportional to the ICE light intensity, denoted by I . We use the photon flux $\Phi = I/(hf_{\text{ion}})$ to write $\Gamma = \sigma\Phi$ with the cross section σ , which has the dimension of a surface. After a total ICE pulse duration T_{ICE} , a measurable consequence of the AI saturation coefficient $\sigma\Phi T_{\text{ICE}}$ is the probability of the atom being autoionized. In the following, this (Rydberg \rightarrow Ion) probability is referred to as the transfer coefficient \mathcal{T} , expressed as

$$\mathcal{T} = 1 - e^{-\sigma\Phi T_{\text{ICE}}}. \quad (1)$$

The ICE light shift is also proportional to I . For spectroscopic measurements, it is more practical to consider the spectral shift $(\Delta f)_{\text{ICE}} = (\Delta E)_{\text{ICE}}/h$ and display the spectral shift per unit light intensity, $(\Delta f)_{\text{ICE}}/I$.

MQDT treats any series of discrete Rydberg levels, i.e., bound states with negative binding energy $E_b < 0$ with respect to the ionization limit, together with the associated continuum of states with positive energy $E_b > 0$, as a single channel. A channel is called closed for energies $E_b < 0$ and open for $E_b > 0$. Interactions between channels are manifested by level perturbations when only closed channels are involved and AI when a closed channel is coupled to an open one: MQDT naturally treats this problem by exhibiting eigenstates of the full Hamiltonian using a restricted set of parameters.

Within a closed channel, E_b is mapped onto an effective quantum number ν according to the quantum defect theory [62] by the Rydberg formula $E_b = -hc\mathcal{R}/\nu^2$, where h is Planck’s constant, c is the speed of light, and \mathcal{R} is the Rydberg constant (corrected for the finite atomic mass). ν is linked to the principal quantum number n in the series with a dimensionless parameter called the quantum defect δ , using the relationship $\nu = n - \delta$. We thus introduce the $6s n_g \ell$ ($6p n_e \ell$) series quantum defect δ_g (δ_e) satisfying $\nu_g = n_g - \delta_g$ ($\nu_e = n_e - \delta_e$) and map the energies E_g , E_e , and E_{ICE} of Fig. 1, respectively, onto ν_g , ν_e , and ν_{ICE} , as follows:

$$E_g = -\frac{hc\mathcal{R}}{\nu_g^2}, \quad (2)$$

$$E_e = hf_{\text{ion}} - \frac{hc\mathcal{R}}{\nu_e^2}, \quad (3)$$

$$E_{\text{ICE}} = hf_{\text{ion}} - \frac{hc\mathcal{R}}{\nu_{\text{ICE}}^2}. \quad (4)$$

In the effective quantum number energy scale (the ν scale), the ICE frequency detuning from ion resonance $f_{\text{ICE}} - f_{\text{ion}}$ is thus mapped onto $\Delta\nu_{\text{ICE}} = \nu_{\text{ICE}} - \nu_g$.

In our two-channel MQDT model, one channel is the $6p\nu_e\ell$ closed channel addressed by ICE and the second is the $6s\epsilon\ell'$ open channel. The coupling to the open channel converts the $6p\nu_e\ell$ channel into a quasicontinuum giving a continuous character to ν_e . All information about the energies and widths of the quasicontinuum are captured by two dimensionless MQDT parameters: δ_e and $R' < 1$, characterizing the quantum defect and the amplitude of the coupling, respectively. The model yields an analytical formula for the AI cross section [62–64] presented in Eq. (A3) of Appendix A. Once the AI cross section is derived, the ICE light shift can be expressed as a principal part integral over the AI rate Γ following a Kramers-Kronig relationship [65,66], yielding Eq. (A5), which is mapped onto an integration over the ν scale in Eq. (A6).

C. Physical predictions and scaling

To illustrate and discuss the predictions of Eqs. (A3) and (A6), in Fig. 2 we show the calculated values of the AI cross section σ and the spectral shift per unit intensity $(\Delta f)_{\text{ICE}}/I$, as a function of f_{ICE} (top axis) and the corresponding $\Delta\nu_{\text{ICE}}$ (bottom), for the Yb $6s60s\ ^1S_0$ Rydberg state (thus $n_g = 60$ and $\ell = 0$), according to our experimental results for δ_e and R' .

We first present the result for σ in Fig. 2(a). The qualitative case $n_e = n_g$ corresponds to the main peak centered around $f_{\text{AI}} \simeq 811.284$ THz (vertical, dotted line), which we call the AI resonance frequency. The AI resonance is slightly detuned (7 GHz to the red) from the ionic core resonance $f_{\text{ion}} \simeq 811.291$ THz (thick vertical scale axis)

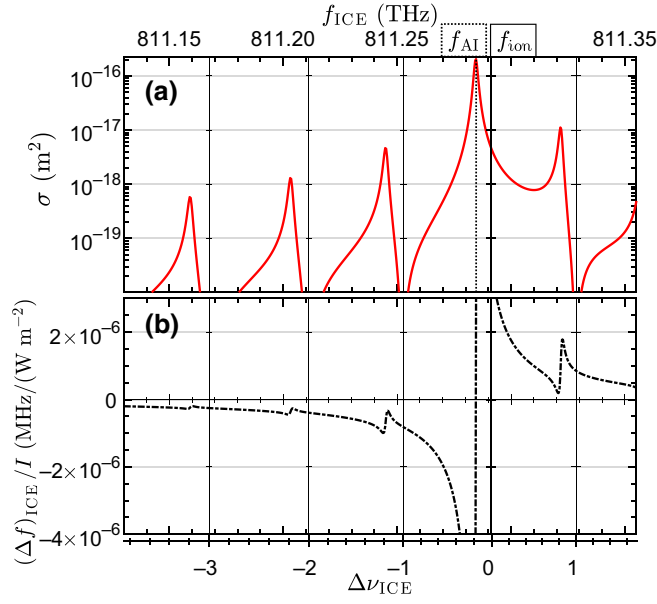


FIG. 2. MQDT theoretical predictions for $6s60s$ 1S_0 Rydberg states using $R' \simeq 0.28$ and $\delta_e \simeq 0.46$ obtained experimentally, as a function of f_{ICE} (top scale) and $\Delta\nu_{\text{ICE}}$ (bottom scale). Regularly spaced vertical axes indicate the ion-core frequency f_{ion} (thick line, $f_{\text{ICE}} \simeq 811.291$ THz or $\Delta\nu_{\text{ICE}} = 0$) or the AIZs (thin lines, $\Delta\nu_{\text{ICE}} \in \mathbb{N}^*$). (a) The AI cross section (full red line). The vertical dotted line marks the cross-section peak at f_{AI} , corresponding to $\Delta\nu_{\text{ICE}} \simeq -0.2$. (b) The spectral ICE shift per unit light intensity (dashed-dotted black line).

because of a small energy mismatch between the binding energies of the Rydberg electron around a $6s$ or a $6p$ ionic core. One can observe significant secondary resonances in the wings of the main peak, known as shake-up satellites [67]. They correspond to the photoexcitation of $6pn_e s$ states with a different principal quantum number $n_e \neq n_g$. Between the shake-up satellites, AIZs appear as a discrete set of frequencies where σ vanishes (thin vertical axes) because of destructive interference between multiple paths to the ionized state [59]. Near-resonant ICE implies a restriction on the range of ICE frequencies, in the form $\Delta\nu_{\text{ICE}} \ll \nu_g \sim n_g, n_e$, which is true in Fig. 2 and more generally in all our measurements. Under this restriction, Eq. (A3) can be approximated with an excellent accuracy by the following expression:

$$\sigma(\nu_{\text{ICE}}, \nu_g) \simeq \frac{2\pi^2 f_{\text{ion}}}{\epsilon_0 c E_H} d^2 \nu_{\text{ICE}}^3 \times A_e^2(\nu_{\text{ICE}} + \delta_e; R') \left[\frac{\sin(\pi \Delta\nu_{\text{ICE}})}{\pi \Delta\nu_{\text{ICE}}} \right]^2, \quad (5)$$

where ϵ_0 is the dielectric constant, E_H is the Hartree energy, and d is the dipole matrix element between ionic core states $6s$ and $6p$. The function A_e^2 given in Eq. (A1) describes the spectral density of the $6p\nu_e\ell$ channel in the

quasicontinuum, with a periodicity of 1 in the ν scale: it contains the location of the AI resonance when $\Delta\nu_{\text{ICE}} = \delta_g - \delta_e$ and of the shake-up satellites. The sinc factor, which originates from an overlap integral between the Rydberg wave functions [60,63,68], captures the AIZs at integral values of $\Delta\nu_{\text{ICE}}$. Note that their positions depend only on the initial state energy and not on R' or δ_e .

Turning to the ICE light shift $(\Delta f)_{\text{ICE}}/I$ displayed in Fig. 2(b), one recognizes the usual feature of $1/\Delta f$ scaling in the wings, where Δf is the detuning from the resonance at f_{AI} and where a rapid sign inversion takes place. Additional fluctuations originate from the AI shake-up satellites. However, they never cancel the light shift. Importantly, at the AIZs, $(\Delta f)_{\text{ICE}}$ is finite: this predicted ability to apply a sizable light shift while avoiding AI has triggered our experimental study of ICE.

Equation (5) combined with the periodicity of A_e^2 shows that $\sigma/\nu_{\text{ICE}}^3$ expressed as a function of $\Delta\nu_{\text{ICE}}$ is independent of ν_g . This scaling thus allows a common presentation of the results of near-resonant ICE for different n_g values merging into a single unified theory. From Eq. (A5), one can infer the same scaling for $(\Delta f)_{\text{ICE}}$, although the approximation is not as good due to the integration inherently violating the near-resonance restriction. Therefore, our shift results performed at different n_g are also displayed as $(\Delta f)_{\text{ICE}}/(\nu_{\text{ICE}}^3 I)$ plotted as a function of $\Delta\nu_{\text{ICE}}$, using a central value for n_g .

III. EXPERIMENTAL INVESTIGATION OF ICE

A. Application to Yb

In this work, we investigate the ^{174}Yb isotope excited in the $6s_{1/2}n_g s$ 1S_0 Rydberg series (thereafter denoted by $6sn_g s$). This series is coupled to the doubly excited series $6p_{1/2}n_e s, J=1$ (denoted by $6pn_e s$) with ICE light close to resonance with the $6s_{1/2} \leftrightarrow 6p_{1/2}$ first optical line of Yb^+ . Figure 3(a) shows all the relevant Yb energy levels involved in our experiment and all the laser-addressed transitions. Although the $6pn_e s$ series couples to two independent continua, it has been demonstrated that a single effective continuum can be considered [64]. We can thus directly apply the results of Sec. II to our particular case. In previous measurements [69], we have determined accurate values for the quantum defect δ_g , with the result $\delta_g \simeq 4.276$. In the following, we use $f_{\text{ion}} = 811.291\,500(40)$ THz [70] for the $6s_{1/2} \leftrightarrow 6p_{1/2}$ ion transition frequency. We also deduce $d = 1.01ea_0$ (where e is the electron charge and a_0 is the Bohr radius) from the Yb^+ $6p_{1/2}$ state natural width, $\Gamma_{sp} = 2\pi \times 19.7$ MHz [71].

B. Experimental setup

Figure 3(b) shows the setup designed for this experiment. The atomic source is based on a magneto-optical

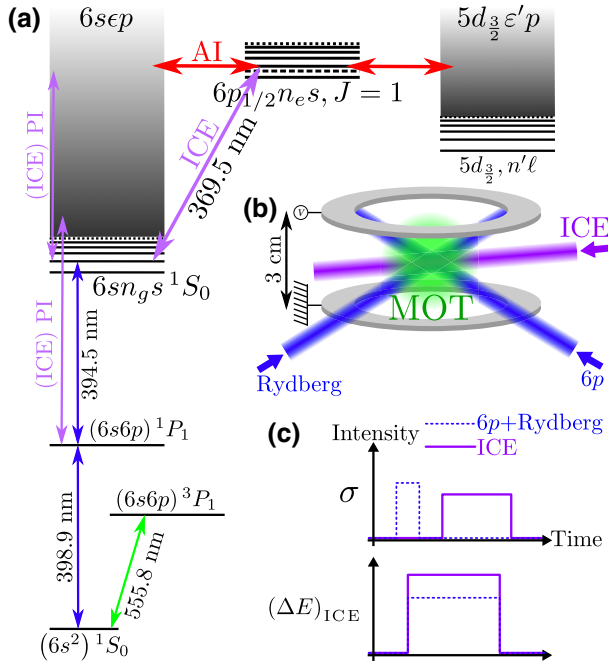


FIG. 3. (a) The energy-level diagram of ^{174}Yb related to the experiment and couplings between them. The purple arrows show the ICE light coupling atoms in $6sn_g s^1S_0$ states to the $6p_{1/2} n_e s, J = 1$ Rydberg series. The red horizontal arrows show the coupling of this doubly excited series to the two continua $6s\epsilon p$ and $5d_{3/2} \epsilon' p$, which are responsible for AI. Possible direct photoionization (PI) processes induced by ICE light are also shown (purple vertical arrows). (b) The laser and electrode configuration around the MOT. (c) The scheme of the laser pulse sequences applied before recording N_{ion} and N_R , for the ICE spectra measurements (yielding the cross section σ) and for the ICE light-shift measurements, yielding $(\Delta E)_{\text{ICE}}$.

trap (MOT) operated on the $(6s^2)^1S_0 \leftrightarrow (6s6p)^3P_1$ intercombination transition at 555.8 nm, described in Ref. [69]. It collects about 10^6 atoms in a sphere of around 1 mm diameter. Three laser excitation beams are shone onto the cold Yb cloud with approximately horizontal propagation. The beams denoted as $6p$ (wavelength 398.9 nm) and Rydberg (394.5 nm) provide two-photon transitions to reach $6sn_g s$ Rydberg states, with $n_g = 50, 60,$ or 72 . The ensemble of atoms excited to Rydberg states, further denoted as the Rydberg cloud, is created in the regime of frozen Rydberg gases [72] in which the Rydberg atoms can interact strongly but have negligible motion on the experimental time scale. The ICE beam at wavelength 369.5 nm couples the $6sn_g s$ state and the $6pn_e s$ series. This light can also induce direct photoionization (PI) (purple vertical arrows in the figure): with the intensities applied during our measurements, PI from $6sn_g s$ states can be neglected but not PI from the $(6s6p)^1P_1$ intermediate state, which has a much higher cross section because the process ends up closer to the first ionization limit.

The $6p$ laser source frequency is locked onto the $(6s^2)^1S_0 \leftrightarrow (6s6p)^1P_1$ optical transition and the $6p$ beam frequency can be detuned from resonance by up to 1 GHz. The Rydberg and ICE laser lights are produced by frequency doubling two dedicated Ti:sapphire sources and their wavelengths are measured by a wave meter with an approximately 1-MHz short-term sensitivity and an approximately 100-MHz long-term accuracy. The Rydberg frequency, denoted by f_{Ryd} , is set by software to any chosen frequency according to the measurement of the wave meter. The ICE frequency f_{ICE} , with lower accuracy requirements (Fig. 2), is tuned manually and left free running between corrections of its drifts, after frequency excursions of typically 100 MHz.

The measurement protocol consists of applying sequences of laser pulses repeated at a 10-Hz rate, with the MOT continuously loaded. The influence of the low-intensity MOT beams (and a Zeeman slower beam used to load the MOT) on the measurement is negligible. The different sequences applied for the measurement of AI spectra or ICE light shifts are illustrated by Fig. 3(c). To measure an AI cross section σ , we first excite atoms to the $6sn_g s$ state with joint resonant pulses of the $6p$ and Rydberg beams; the ICE light is applied shortly afterward to test for possible AI. The AI spectra are obtained after measuring the variations of σ with f_{ICE} , typically scanned over several tens of gigahertz (see Fig. 2). On the contrary, to measure the ICE light shift, the three laser beam pulses are applied simultaneously and the duration of all the light pulses is thus T_{ICE} . The $6sn_g s$ level shift is manifested as a shift of the Rydberg-excitation resonance frequency while maintaining f_{ICE} constant and scanning f_{Ryd} (typically over 50 MHz) around the excitation resonance. The spectral shift per unit intensity $(\Delta f)_{\text{ICE}}/I$ is eventually deduced after data analysis.

After each pulse sequence, an electric field ramp ionizes Rydberg states and sends all the ions toward a microchannel plate (MCP) for counting. The MCP gain provides a single ion signal of around 0.2 V over 100 ps, corresponding to an average integrated signal of around 2×10^{-11} V s. Ions already present at the end of the laser pulse sequence are discriminated from those due to ionized Rydberg atoms by their time of flight. Gated integration of the MCP signals thus yields the number of ions N_{ion} and the number of Rydberg atoms N_R at the end of the pulse sequence.

C. Experimental parameters

The transverse sizes of the three beams at the Rydberg-cloud location, described by the waist radii w_{6p} , w_{Ryd} , and w_{ICE} , are adjusted according to our needs for the different measurements. For AI spectra measurements, the joint $6p$ plus Rydberg-excitation pulse is applied for typically $0.5 \mu\text{s}$, followed by a $0.5\text{-}\mu\text{s}$ lag time before the ICE pulse.

TABLE I. Typical values for relevant experimental parameters over the different measurements. “(R)” and “(B)” denote, respectively, the red- or blue-detuned AIZs. For w_R , we display typical values obtained after data analysis.

	ICE spectra	Shift out of AIZ		Shift on AIZ	
n_g	50/60	50/60	72	72 (R)	72 (B)
$T_{\text{ICE}} (\mu\text{s})$	4.2	2.25	3	6	
$w_{\text{ICE}} (\mu\text{m})$	560	83		105	
$w_{6p} (\mu\text{m})$	300	300		80	
$w_{\text{Ryd}} (\mu\text{m})$	500	200		200	
$w_R (\text{fit}) (\mu\text{m})$	400	300		120	200

The ICE pulse duration T_{ICE} is summarized in Table I. Consequently, the whole sequence lasts at most 6 μs before detection, which is significantly lower than the $6sn_g s$ -state lifetime.

Attention is paid to accurate knowledge of the ICE beam properties. Mode cleaning is achieved through a single-mode fiber and its intensity distribution is checked using a CCD camera. The ICE light polarization is linear in the horizontal direction and its total power, $P_{\text{ICE}} \sim 20\text{--}50$ mW, is measured using a photodiode-based power meter prior to each measurement.

Table I summarizes the values of the relevant parameters applied during our measurement campaign. Also introduced is a Rydberg-cloud waist w_R , assuming a Gaussian shape for the Rydberg-atom density distribution: w_R is

deduced from data analysis (Appendices B and C). Indeed, we find that it is important to account for the finite size of the Rydberg cloud in order to evaluate the AI cross section and shift accurately. The table displays typical values obtained, which appear to be consistently compatible with w_{6p} and w_{Ryd} .

IV. AI SPECTRA

We first record AI spectra to obtain the MQDT parameters describing the properties of the $6pn_{e}s$ Rydberg series and confirm the existence of AIZs. The signal is maximized by creating large Rydberg clouds and the ICE beam waist w_{ICE} is chosen accordingly (see Table I). These AI spectra are very similar to those of the previous investigations of ICE using atomic beams [49,59,60,63,67,68,73,74]. Here, effort is directed toward the frequency resolution of the spectra, the quantitative evaluation of the AI cross section, and its reduction near the AIZs. We record N_{Ion} and N_R as a function of f_{ICE} and compute the measured ionization probability:

$$\mathcal{T}_{\text{exp}} = \frac{N_{\text{Ion}}}{N_{\text{Ion}} + N_R}. \quad (6)$$

Figure 4 shows the rescaled cross sections derived after analysis of ICE spectra $\mathcal{T}_{\text{exp}}(f_{\text{ICE}})$ measured for $n_g = 50$ and $n_g = 60$, in the framework introduced in Sec. II C. They are compared with the predictions of the MQDT model displayed as σ_{MQDT} , which is computed using

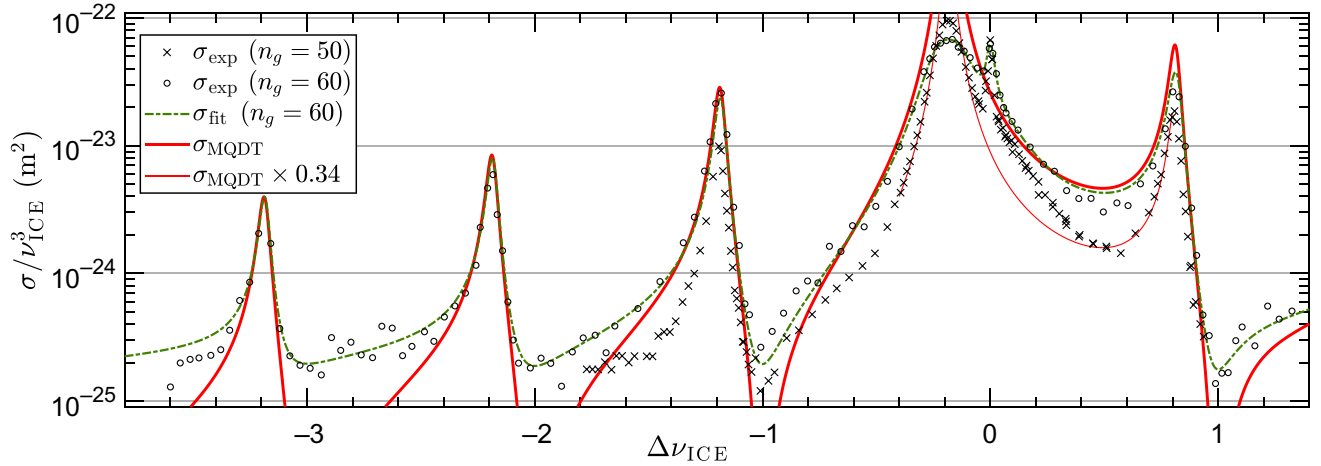


FIG. 4. Results of AI-spectra measurements, displayed as overall ionization cross sections σ_{exp} rescaled by $1/v_{\text{ICE}}^3$ for $n_g = 50$ (crosses) and $n_g = 60$ (circles). Each data point corresponds to the average over 100–500 measurements. The cross section σ_{fit} (dashed-dotted green line), fitted from the experimental $n_g = 60$ ionization probability \mathcal{T}_{exp} , is plotted together with the theoretical cross section σ_{MQDT} (thick red plain line) computed from the fitted values of R' and δ_e for comparison. The peak value predicted for the AI cross section at the AI resonance, $\Delta\nu_{\text{ICE}} \simeq -0.19$, is $\sigma/v_{\text{ICE}}^3 = 1.2 \times 10^{-21}$ m^2 and corresponds to a saturation coefficient $\sigma\Phi T_{\text{ICE}} \sim 50$ (see Sec. II B). The $n_g = 50$ AI cross section is found to be smaller than the theoretical predictions by a factor $\simeq 0.34$: for comparison, we also plot a reduced theoretical MQDT cross section (thin red line). The $n_g = 50$ data exhibit an additional pedestal centered at $\Delta\nu_{\text{ICE}} = 0$, manifested as a mismatch between σ_{exp} and $\sigma_{\text{MQDT}} \times 0.34$: it is interpreted as a Förster resonant energy transfer (Appendix B).

Eq. (A3) and with the values of R' and δ_e deduced from our data analysis. We note that σ_{MQDT} already grasps the essence of the physics involved, being parametrized with just R' and δ_e . σ_{fit} maps the simulation of \mathcal{T}_{exp} obtained after our best-fit procedures: this simulation includes σ_{MQDT} and corrections that capture the effects of the finite Rydberg-cloud size and of experimental defects. More details about the data analysis and the exact quantities plotted can be found in Appendix B.

For $n_g = 60$, we find excellent agreement between the experimental and theoretical cross sections over several orders of magnitude. For $n_g = 50$, we observe a cross section with the correct qualitative behavior but three times smaller than predicted. The best-fit procedures yield the values $R' \simeq 0.28$ and $\delta_e \simeq 0.46$ (modulo 1) for the MQDT parameters, with less than 10^{-2} relative difference between the $n_g = 50$ and $n_g = 60$ values and relative uncertainties in the 10^{-2} range for R' and in the 10^{-3} range for δ_e : this stability excludes the presence of an additional strongly perturbing channel and validates the two-channel approach. Clearly visible are the strong shake-up satellite peaks arising from nearby members of the $6pn_e s$ series.

Apart from the apparent reduction of the AI cross section for $n_g = 50$, other deviations between σ_{exp} and σ_{MQDT} are exhibited in Fig. 4. First, we find a finite offset value for σ_{exp} at the locations of the AIZs. Second, we observe a saturation of σ_{exp} at the AI resonance peak ($\Delta\nu_{\text{ICE}} = \delta_g - \delta_e \simeq -0.2$): $\sigma_{\text{exp}} < \sigma_{\text{MQDT}}$ (or $\sigma_{\text{exp}} < \sigma_{\text{MQDT}} \times 0.34$ for $n_g = 50$). Finally, a more intriguing feature is the narrow peak in the cross section at the ionic core resonant frequency $\Delta\nu_{\text{ICE}} = 0$, not predicted by the MQDT model, and an additional pedestal for $n_g = 50$. All the deviations are successfully ascribed to plausible experimental defects and are accounted for by fitted corrections in the simulations, as illustrated by the excellent agreement between σ_{exp} and σ_{fit} (displayed only for $n_g = 60$ for clarity). Our measurements are thus compatible with MQDT predictions. We now focus on finite AI, which is critical for applications, while explanations of the other deviations can be found in Appendix B.

For f_{ICE} tuned within approximately 100 MHz around an AIZ, we measure an apparent residual ionization cross section $\sigma_{\text{exp}}/\nu_{\text{ICE}}^3 \sim 10^{-25} \text{ m}^2$. We ascribe it to the PI of a small fraction of atoms excited to the $(6s6p) {}^1P_1$ state (see Fig. 3) by the Zeeman slower beam. To test this claim, we verify that we detect the same ion signal whether or not the $6p$ and Rydberg beams are applied. Moreover, this residual ion count appears to be independent of f_{ICE} within the range experimentally tested. Within our experimental uncertainty, our measurements thus confirm the existence of the AIZs predicted by the MQDT model, appearing as deep minima where the AI cross section is reduced, as compared to the AI resonance, by a factor of at least 10^4 .

V. ICE LIGHT SHIFT

To test for the existence of a shift imparted by ICE light to $6sn_g s$ states and compare it with the value predicted by MQDT, we perform Rydberg-excitation spectroscopy under ICE illumination by recording N_{Ion} and N_R while varying f_{Ryd} (see Sec. III B and Fig. 3c). We test the principal quantum numbers $n_g = 50, 60$, and 72 and various values of f_{ICE} within a range corresponding to $-1.2 \lesssim \Delta\nu_{\text{ICE}} \lesssim 1.0$. The Rydberg-cloud size is reduced in order to allow for smaller ICE beam waists and thus increased shifts (Table I). Note that the absolute ground state as well as the intermediate 1P_1 state undergo negligible ICE light shifts under our experimental conditions. For each measurement, the spectral shift $(\Delta f)_{\text{ICE}}/I$ is extracted as a best-fit value using simulations of the joint signals $N_{\text{Ion}}(f_{\text{Ryd}})$ and $N_R(f_{\text{Ryd}})$: more details about this data analysis can be found in Appendix C. Two different approaches are used depending on whether or not an AI signal is detectable.

A. Light-shift measurements away from the AIZs

Rydberg-excitation spectroscopy with the ICE laser tuned away from the AIZs is performed observing both N_{Ion} and N_R . Atoms in the center of the ICE beam are exposed to the highest ICE intensity and have the largest shifts and AI rates, while atoms near the edges of the beam experience small intensity and are negligibly shifted or ionized. Therefore, with the ICE beam strongly focused on a small fraction of the Rydberg cloud, we expect N_{Ion} to present a strong asymmetry as compared to N_R .

Figure 5 presents one measurement obtained with $n_g = 50$ and $\Delta\nu_{\text{ICE}} \simeq -0.365$. A strong Rydberg signal is visible and serves qualitatively as a frequency reference for the ion signal. The obvious asymmetry in the ion signal characterizes the range of ICE light shifts applied throughout the ICE beam in the Rydberg cloud. The simulation reproduces both signals well and best fits yield a measured shift $(\Delta f)_{\text{ICE}}/I \simeq (-3.10 \pm 0.25) \times 10^{-6} \text{ MHz}/(\text{W m}^{-2})$ (statistical uncertainties for 1σ confidence band). The value predicted by the MQDT model is $(\Delta f)_{\text{ICE}}/I = -2.20 \times 10^{-6} \text{ MHz}/(\text{W m}^{-2})$. The mismatch is attributed in part to experimental fluctuations such as the ICE laser power, the MOT position, and the wave meter stability and in part to the limitations of the model that is used to simulate the signals, also discussed in Appendix C.

With the experimental parameters detailed in Fig. 5, the waist size $w_{\text{ICE}} = 83 \mu\text{m}$ (Table I) and according to the results of the fit, a Rydberg atom at the center of the ICE beam lies within a deep trap associated with a negative level shift of 12 MHz: this value can be approximately deduced by observing the ion-signal cutoff highlighted by the inset in Fig. 5 directly.

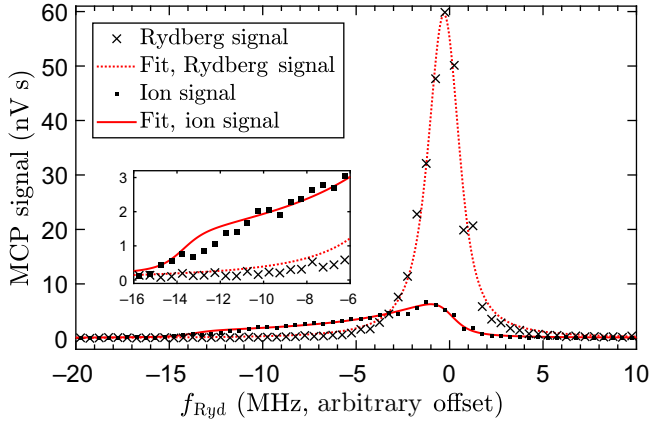


FIG. 5. Rydberg-excitation spectroscopy with $n_g = 50$ and f_{ICE} tuned to $\Delta\nu_{\text{ICE}} \simeq -0.365$: recorded Rydberg (crosses) and ion (squares) signals as a function of the Rydberg-excitation laser frequency f_{Ryd} . Measurements are binned over a frequency range of 250 kHz, each data point corresponding to the average over 50–100 measurements. The simulation (dotted and plain lines) uses the AI cross section $\sigma \simeq 6.14 \times 10^{-19} \text{ m}^2$ obtained from the $n_g = 50$ AI spectrum and the applied ICE total power $P_{\text{ICE}} = 43 \text{ mW}$. The inset shows an enlargement of the cutoff of the ion signal, corresponding approximately to the highest ICE spectral shift $(\Delta f)_{\text{ICE}}$ at the beam center.

B. Light-shift measurements at the AIZs

With the ICE laser tuned to an AIZ, the signal due to AI is too weak and the procedure previously depicted to deduce the light shift by comparison between the Rydberg and ion signals is ineffective. Instead, we compare the Rydberg signals obtained with and without the ICE light after implementing shot-to-shot alternation of the ICE pulse application.

In order to apply a significant shift to all atoms, we reduce the size of the Rydberg cloud further and increase w_{ICE} slightly (Table I). We also detune the $6p$ laser frequency by 1 GHz from the $^1S_0 \leftrightarrow ^1P_1$ resonance in order to reduce both the frequency width of the Rydberg-excitation profile and the background ion signal stemming from the direct PI of atoms in the 1P_1 state. T_{ICE} is extended to $6 \mu\text{s}$ to preserve the overall signal.

Figure 6 shows the signals recorded for $n_g = 72$ at the first red- and blue-detuned AIZs ($\Delta\nu_{\text{ICE}} = \pm 1$). They show clear shifts of the Rydberg-excitation resonance frequency, in opposite directions. At the red zero (left panel), the best fit yields a shift $(\Delta f)_{\text{ICE}}/I \simeq (-1.62 \pm 0.04) \times 10^{-6} \text{ MHz}/(\text{W m}^{-2})$, while the predicted shift is $-1.46 \times 10^{-6} \text{ MHz}/(\text{W m}^{-2})$. A small excess ion signal of about 2% of the Rydberg signal is also visible, corresponding to a residual AI cross section $\sigma_{\text{exp}} \simeq 4 \times 10^{-21} \text{ m}^2$ ($\sigma_{\text{exp}}/\nu_{\text{ICE}}^3 \simeq 1.4 \times 10^{-26} \text{ m}^2$), about 5 orders of magnitude below the peak AI cross section. It is consistent with a residual mismatch of f_{ICE} with the AIZ, within the observed frequency drift due to the free-running operation

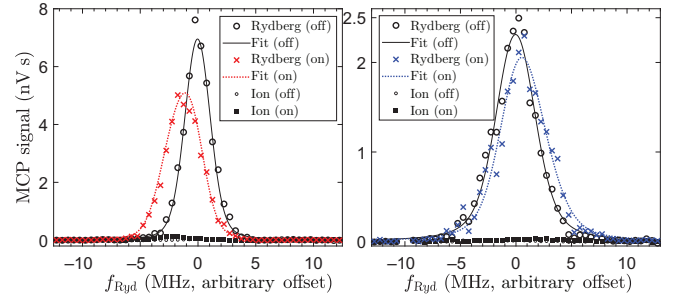


FIG. 6. The evidence for an ICE shift at the AIZs obtained for $n_g = 72$: “on” and “off” denote the application of the ICE beam. The measurements are binned over a frequency range of 250 kHz, each data point corresponding to the average over 100–200 measurements. The fits (lines) display the simulations that model both signals simultaneously (Appendix C 1). Left: the first red-detuned AIZ ($\Delta\nu_{\text{ICE}} = -1$) recorded with $P_{\text{ICE}} = 34 \text{ mW}$. The best fit to the data yields $(\Delta f)_{\text{ICE}}/I \simeq (-1.62 \pm 0.04) \times 10^{-6} \text{ MHz}/(\text{W m}^{-2})$, while the predicted shift is $-1.46 \times 10^{-6} \text{ MHz}/(\text{W m}^{-2})$. Right: the first blue-detuned AIZ ($\Delta\nu_{\text{ICE}} = +1$) recorded with $P_{\text{ICE}} = 29 \text{ mW}$, resulting in the fitted value $(\Delta f)_{\text{ICE}}/I \simeq (+2.1 \pm 0.25) \times 10^{-6} \text{ MHz}/(\text{W m}^{-2})$ [predicted $+1.50 \times 10^{-6} \text{ MHz}/(\text{W m}^{-2})$].

of the ICE laser source (Sec. III B). Frequency locking of this laser source should readily correct this defect and ensure the absence of AI.

At the blue zero (right panel), the simulation yields a shift $(\Delta f)_{\text{ICE}}/I \simeq (+2.1 \pm 0.25) \times 10^{-6} \text{ MHz}/(\text{W m}^{-2})$ and the predicted shift is $+1.5 \times 10^{-6} \text{ MHz}/(\text{W m}^{-2})$. No excess ion signal is clearly visible there. We consider its typical standard deviation as an upper bound, yielding a maximum transfer coefficient of 0.4%, corresponding to a reduction of almost 6 orders of magnitude of the AI rate as compared to the ICE AI resonance. The lifetime without AI is then estimated to be longer than 1 ms, much larger than the Rydberg-state radiative lifetime.

Manipulation of the core electron without disturbing the Rydberg electron was utilized to reach higher excited levels of the core with a multiphoton transition [75] through an AIZ of a doubly excited Rydberg intermediate state. However, to our knowledge, no demonstration of an ICE light shift has previously been reported, in particular at an AIZ. Figure 6 confirms the possibility of applying a strong ICE light shift to an atom in a Rydberg state without AI. Focusing the ICE beam to $w_{\text{ICE}} = 10 \mu\text{m}$, a strong shift of around 100 MHz is expected with only 10 mW. It can be used either to apply a force or engineer the quantum state phase, without loss or decoherence.

C. Light shift as a function of the detuning

For an overall comparison between our light-shift measurements and the predictions of the MQDT model, we gather the shifts obtained for different n_g numbers using the

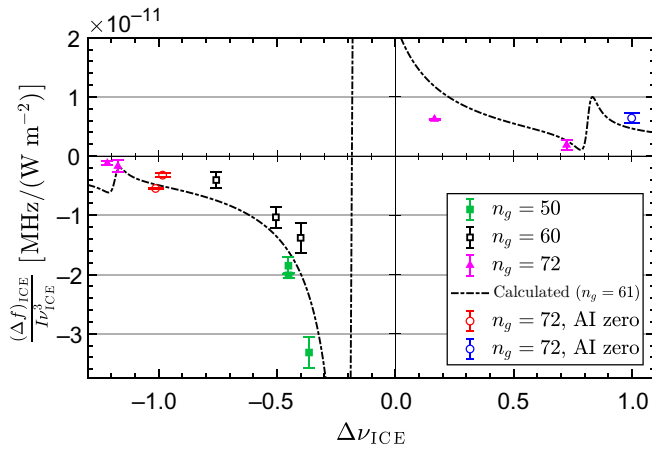


FIG. 7. The ICE light shift per unit intensity, rescaled by $1/\nu_{\text{ICE}}^3$, extracted from Rydberg-excitation spectroscopy at $n_g = 50, 60$, and 72 . The dashed-dotted line presents the theoretical shift for $n_g = 61$ using Eq. (A6).

same $1/\nu_{\text{ICE}}^3$ rescaling as for the AI cross section. Figure 7 thus presents the values of $(\Delta f)_{\text{ICE}} / (\nu_{\text{ICE}}^3 I)$ obtained for all our light-shift measurements as a function of $\Delta\nu_{\text{ICE}}$. We remind the reader of the residual dependence of this quantity on n_g (Sec. II C) and choose to display the theoretical shift for $n_g = 61$. The displayed error bars are the statistical uncertainties (1σ confidence bands) yielded by the data-fitting procedure.

We find satisfactory agreement between the measured shifts and calculations and the predicted evolution with $\Delta\nu_{\text{ICE}}$ is also well verified. The residual disagreement, which clearly exceeds statistical uncertainty, is well explained by the limitations of the simulations (Appendix C 3) and the level of stability of the laser powers, the wave meter measurements, and the MOT position. Presumably owing to this experimental uncertainty, the predicted influence of the shake-up satellites on the shift is only partially confirmed by our measurements. Nevertheless, Fig. 7 confirms that the ICE light shift imposed on Rydberg atoms follows the predictions of the MQDT model.

VI. DISCUSSION AND CONCLUSIONS

The AI spectra together with the Rydberg-excitation spectroscopy at the AIZs exhibit a dramatic reduction of orders of magnitude of the AI rate and the possibility of using near-resonant ICE for coherent operations on low- ℓ Rydberg states of alkaline-earth species. Experimentally, AIZs are easily accessed, with the requisite frequency accuracy well within the reach of common experimental apparatus. The near-resonant character enables the creation of strong shifts that are selectively applied to Rydberg states and drastically reduces the light power needed. The

short wavelength also implies possible improvements of the spatial resolution when tailoring the ICE intensity distribution.

The minimal decoherence attainable when using ICE deserves inspection. An inevitable source of residual decoherence obviously arises from inclusion of the finite core-electron radiative decay. In the presented MQDT model, PI is neglected; however, its inclusion would not prevent ionization zeros from existing but only induce a small modification of their position as compared to $\Delta\nu_{\text{ICE}} = \pm 1$, according to the studies of Fano-Beutler profiles [65,76]. Accounting for more channels may lead to nonzero AI rates [64]. This extension might be necessary for the treatment of far-from-resonance ICE or for configurations involving strong perturbations between Rydberg levels in different series. For example, the $6p_{1/2}v_e s$ channel of the bosonic ^{174}Yb , which has no nuclear spin, can in places be perturbed by the ^{174}Yb $6p_{3/2}v_e s$ channel but series converging to higher ionization limits have minimal influence except for coincidental resonances [77]. The case of fermionic atoms displaying hyperfine splittings (thus several series with very close ionization limits), which is particularly interesting for quantum operations [78], deserves thorough investigation.

The systematic recording of AI spectra for an extended range of n_g numbers should yield important information about possible perturbing channels, which in turn will improve the accuracy of MQDT predictions. Along the same lines, with regard to the prospect of applying ICE to Rydberg states with higher total angular momentum (J or F quantum number), in general, more channels must inevitably be accounted for. Systematic studies with high- ℓ states [55,57,79], but also with excitations of the core above the first optical line [75], possibly up to the most interesting double Rydberg states [79–84], should provide valuable insights. These may prove crucial in the engineering of advanced quantum operations with these states or the investigation of AI with far-off-resonance ICE [48,54], where the consistency of the MQDT model is still to be verified. In the most optimistic case, the decoherence is presumably reduced to the radiative decay rate of the ionic core, as it is for circular states.

Near-resonant ICE is a new tool offered for experiments aimed at quantum information processing. It will enable the trapping of Rydberg states, which is expected to improve the fidelity of quantum operations [12,47,54]. It will also bring a new degree of freedom for local addressing or phase engineering [23–26,85–87], which leaves the ground-state trapping potential untouched. For instance, one could entangle distant pairs with strong ICE shifts to tune the Rydberg resonances while leaving in-between atoms unperturbed. In this manner, one can expect multiplication of the connectivity of quantum operations [14,24] or the realization of elaborate quantum gates with more than two qubits.

By choosing the ICE light detuning, one can switch between complementary actions, namely the coherent application of a shift or fast AI with a very high certainty. The latter can also be used for the development of technologies for the manipulation of quantum information. At the present time, near-resonant ICE has only been used to ensure the absence of false detection with optical imaging of ground-state atoms [47]. However, the implementation of a joint detection of atoms by optical means, and of single ions with a high detectivity using common electron-multiplying devices, seems within the reach of current apparatus in the near future. Within this framework, implementation of ion optics should strengthen the detection of correlations. Finally, the use of AI can constitute a new pathway to engineer samples of ions trapped in optical tweezers with ultimate control [47].

ACKNOWLEDGMENTS

We acknowledge useful discussions with Eliane Luc-Koenig, Sylvain Schwartz, and Hans Lignier. This work benefited from financial support by the Laboratoire d'Excellence, Physique Atomes Lumière Matière (LabEx PALM) (Grant No. ANR-10-LABX-0039-PALM). S.L. acknowledges the additional support of the Centre national de la recherche scientifique (CNRS) through the program "Tremplin@INP 2021".

APPENDIX A: TWO-CHANNEL MQDT MODEL

In this appendix, we provide details about the predictions of the effects of ICE light according to the two-channel MQDT model introduced in Sec. II. We rely on the conceptual and mathematical frameworks introduced in Secs. II A and II B, introducing the definitions of the effective quantum numbers and quantum defects. Note that a rigorous illustration of the concept of channel in Figs. 1 and 3 would necessitate associating the $6sn_g\ell$ series with the continuum $6s\epsilon'\ell$ and the continuum $6s\epsilon\ell'$ with the $6sn\ell'$ series. As $6s\epsilon'\ell$ and $6sn\ell'$ series are not addressed when using ICE, we take the opportunity to simplify the figures, merging the two independent channels which present a common ionization limit.

MQDT allows us to obtain an analytical formula for the spectral density A_e^2 of the $6p\nu_e\ell$ channel within the quasicontinuum resulting from the coupling of the $6p\nu_e\ell$ and $6s\epsilon\ell'$ channels. It is given (in ν scale) by the following function [62–64]:

$$A_e^2(\nu_e, \delta_e, R') = R'^2 \left(\frac{1 + \tan^2[\pi(\nu_e + \delta_e)]}{R'^4 + \tan^2[\pi(\nu_e + \delta_e)]} \right), \quad (\text{A1})$$

where we exhibit the dependence on ν_e , while δ_e and R' are the constant MQDT parameters characterizing the two channels. The spectral density is periodic with period 1

and verifies $\int_{\nu_0-1}^{\nu_0} A_e^2 d\nu_e = 1$, which ensures overall state-density conservation when the two channels are mixed. Its maximum value is $1/R'^2$, which occurs when $\nu_e + \delta_e$ is an integer. If we focus on the regime in which $\nu_e + \delta_e$ is small, it is straightforward to show that $A_e^2(\nu_e)$ is, to a good approximation, a Lorentzian peaked at $\nu_e = -\delta_e$ with a width (full width at half maximum, FWHM) $\Delta\nu_e$ given by Ref. [64]:

$$\Delta\nu_e = \frac{2R'^2}{\pi}, \quad (\text{A2})$$

which corresponds to the $1/\nu_e^3$ energy scaling of the widths evoked in Sec. II A.

The measurement of an AI spectrum consists in scanning E_{ICE} over the $6p\nu_e\ell$ channel, while recording AI as a signature of photoexcitation. Within our framework, the AI cross section $\sigma(E_{\text{ICE}}, E_g) = \sigma(\nu_{\text{ICE}}, \nu_g)$ is evaluated by considering laser excitation from a bound $6sn_g\ell$ Rydberg state, with effective quantum number ν_g , to the $6p\nu_e\ell$ channel: here, we thus consider specifically the energy level $E_e = E_{\text{ICE}}$, and accordingly $\nu_e = \nu_{\text{ICE}}$, and use the ICE approximation to obtain the following expression for $\sigma(\nu_e, \nu_g)$ [62–64]:

$$\sigma(\nu_e, \nu_g) = \frac{2\pi^2 f_{\text{ion}} d^2}{\epsilon_0 c E_H} A_e^2(\nu_e; \delta_e, R') f(\nu_e, \nu_g), \quad (\text{A3})$$

with

$$f(\nu_e, \nu_g) = \nu_e^3 \frac{4\nu_e\nu_g}{(\nu_e + \nu_g)^2} \left[\frac{\sin[\pi(\nu_e - \nu_g)]}{\pi(\nu_e - \nu_g)} \right]^2 \quad (\text{A4})$$

and with the constants f_{ion} , d , ϵ_0 , c , and E_H already defined in Sec. II. In Eq. (A3), $A_e^2\nu_e^3/E_H$ is the spectral density in energy units. The ICE approximation considers that the electric dipole operator from the ICE light acts only on the core electron. The laser coupling is then expressed by the product of d^2 with the squared overlap integral $f(\nu_e, \nu_g)/\nu_e^3$ between the two Rydberg wave functions of the spectator electron [68], the latter is the source of the AIZs in the ICE approximation within the MQDT approach. The apparent contradiction between Refs. [59] and [60] on the origin of the AIZs lies at the heart of the MQDT, which directly considers the $6p\nu_e\ell$ channel wave functions, which could also be expressed as a sum over the discrete $6pn_e\ell$ Rydberg-state wave functions constituting a basis. In the discrete-states picture evoked in Sec. II C, the AIZs are naturally envisioned as an interference between the contribution of the discrete states to the autoionization, while MQDT provides the relevant linear combination right away and the interference is revealed in the oscillating overlap integral. In this squared overlap integral, the prefactor $4\nu_e\nu_g/(\nu_e + \nu_g)^2$ is very close to 1 when

we restrict to the near-resonance condition $\nu_{\text{ICE}} = \nu_e \simeq \nu_g$; hence Eq. (5) obtained from Eq. (A3) when $\text{inf}(\nu_e, \nu_g)/\nu_e^3$ only the sinc function remains.

We now evaluate the ICE light shift on the $6sn_g\ell$ Rydberg state. By considering AI as a direct relaxation to the continuum, $(\Delta E)_{\text{ICE}}$ and the AI rate $\Gamma(E_e, E_g) = \sigma(\nu_e, \nu_g) \Phi$ are linked by the Kramers-Kronig relationship [65,66]:

$$(\Delta E)_{\text{ICE}} = \mathcal{P} \left\{ \int_{-\infty}^{+\infty} dE_e \frac{\hbar \Gamma(E_e, E_g)}{2\pi E_{\text{ICE}} - E_e} \right\}, \quad (\text{A5})$$

where \mathcal{P} indicates the Cauchy principal value of the integral. In contrast to the case of real photoexcitation for which Eqs. (A1) and (A3) use $E_e = E_{\text{ICE}}$, to calculate $(\Delta E)_{\text{ICE}}$ at a fixed energy E_{ICE} , we now have to integrate $\Gamma(E_e, E_g)$ over the whole energy range for E_e . The change of integration variable from E_e to ν_e yields the following expression, which exhibits the direct scaling of $(\Delta E)_{\text{ICE}}$ with the ICE light intensity I :

$$(\Delta E)_{\text{ICE}} = \frac{Id^2}{2\epsilon_0 c E_H} \mathcal{P} \left\{ \int_0^{+\infty} d\nu_e \frac{g(\nu_e) A_e^2}{\nu_{\text{ICE}} - \nu_e} \right\}, \quad (\text{A6})$$

with

$$g(\nu_e, \nu_g, \nu_{\text{ICE}}) = \frac{8\nu_g \nu_e^3 \nu_{\text{ICE}}^2}{(\nu_e + \nu_{\text{ICE}})(\nu_g + \nu_e)^2} \times \left[\frac{\sin[\pi(\nu_e - \nu_g)]}{\pi(\nu_e - \nu_g)} \right]^2. \quad (\text{A7})$$

The light shift can be seen as the consequence of virtual transitions between the initial state and excited states, leading to a shift structured with the satellite peaks.

APPENDIX B: ANALYSIS OF AI SPECTRA AND DATA PRESENTATION

1. Physical model with a finite Rydberg-cloud size

As introduced in Sec. III C, the simulations of the signals obtained during AI-spectra and ICE light-shift measurements account for the finite size of the Rydberg cloud, described with an effective waist radius w_R assuming a Gaussian shape for the Rydberg-atom density distribution. For the AI spectra, this inclusion appears as a correction improving the accordance between σ_{exp} and σ_{fit} in Fig. 4, because the Rydberg-cloud waist w_R is smaller but close to w_{ICE} , with the result that the ICE light intensity varies moderately but not negligibly over the cloud size. As described in Appendix C, the light-shift measurements involve tightly focused ICE beams and this inclusion proves to be fundamental. Here, we give details about the assumptions of the model and the derivations implied,

which are also useful for presentation of the simulations of light-shift measurements.

We now consider the specific case of AI spectra, for which the Rydberg cloud is created prior to the ICE illumination. Before the ICE pulse, the Rydberg-atom density $n_{R,0}$, driven by the combined properties of the $6p$ and Rydberg beams and their overlap, is *a priori* unknown. We first integrate the density along the ICE beam propagation axis and consider a surface distribution for $n_{R,0}$, illuminated by the following—well calibrated—ICE light intensity of Gaussian profile:

$$I(r) = \frac{2P_{\text{ICE}}}{\pi w_{\text{ICE}}^2} e^{-2r^2/w_{\text{ICE}}^2}, \quad (\text{B1})$$

where r is the distance to the beam center. The Rydberg-density integration is justified by the negligible absorption of the light by the low-density Rydberg cloud and by the long Rayleigh length of the ICE beam as compared to the MOT size. We assume that the ICE beam is well centered on the Rydberg cloud. Without supplementary knowledge about its (integrated) shape, a reasonable guess for the surface density $n_{R,0}$ is to consider a Gaussian axisymmetric distribution:

$$n_{R,0}(r) = \frac{2N_{\text{tot}}}{\pi w_R^2} e^{-2r^2/w_R^2}, \quad (\text{B2})$$

where N_{tot} is the total number of Rydberg atoms created. Note that in general, w_R is not equal to the waist radius of the Rydberg beam w_{Ryd} .

To calculate the overall ion and Rydberg signals obtained after the autoionizing ICE pulse within this framework, one has to compute the local ionization probability \mathcal{T} (or the complementary survival probability in a Rydberg state $1 - \mathcal{T}$) for an atom at position r , by applying Eq. (1) with the local ICE photon flux $\Phi(r) = I(r)/(hf_{\text{ion}})$. In this manner, at the end of the ICE pulse, the density of the remaining Rydberg atoms is $n_{R,0} \exp[-\sigma \Phi(r) T_{\text{ICE}}]$ and the complementary signals are obtained by surface integration:

$$N_R = \frac{2N_{\text{tot}}}{\pi w_R^2} \int_0^\infty 2\pi r dr e^{-2r^2/w_R^2} e^{-\sigma \Phi(r) T_{\text{ICE}}} \\ N_{\text{Ion}} = N_{\text{tot}} - N_R, \quad (\text{B3})$$

which yields an expression for the overall survival probability N_R/N_{tot} in the form of an incomplete gamma function; Eq. (1) is naturally retrieved when $w_R \ll w_{\text{ICE}}$, where Φ is the maximal photon flux at the center of the beam.

2. Parametrization and best-fit procedures

We simulate the recorded AI spectra $\mathcal{T}_{\text{exp}}(f_{\text{ICE}})$ computed from experimental data [Eq. (6)] by calculating

the overall transfer coefficient defined after Eq. (B3) and correcting it to account for various, predictable or observed, residual experimental defects, yielding the simulated transfer \mathcal{T}_{fit} .

The simulation is parametrized as follows. Six parameters corresponding to controlled, measured, or already known quantities are included as constants: the n_g quantum number and the corresponding quantum defect δ_g ; the ionic core resonant frequency f_{ion} ; the properties of the ICE light distribution, defined by the total beam power P_{ICE} and the waist radius on the Rydberg cloud w_{ICE} ; and the ICE pulse length T_{ICE} . Nine supplementary parameters are adjusted by the best-fit procedure:

- (1) The fundamental parameters of the MQDT model, δ_e and R' , are naturally included within the description of the cross section σ .
- (2) The Rydberg-cloud size w_R , is physically retrieved through the fit due to the knowledge of w_{ICE} .
- (3) The background ion signal observed as an offset in \mathcal{T}_{exp} , and the saturation of the transfer coefficient to a value less than 1 ($\sigma_{\text{exp}} < \sigma_{\text{MQDT}}$ at the AI resonance) are each described by a coefficient that directly corrects \mathcal{T}_{fit} .
- (4) The supplementary ion-signal peak at the ion resonance frequency is treated as a supplementary Lorentzian ionization cross section centered on f_{ion} , characterized by two parameters, the amplitude and the spectral width.
- (5) Similarly, two supplementary parameters also simulate an extra cross section of Gaussian shape, centered on f_{ion} , to capture the observed pedestal at $n_g = 50$.
- (6) Finally, for the $n_g = 50$ spectra only, a supplementary parameter is included as an overall scaling factor for the AI cross section, yielding the value 0.34.

3. Experimental defects assignment

We have already ascribed the background ion signal to the PI of atoms in $(6s6p) \ ^1P_1$ states (Sec. IV) due to a test in the absence of Rydberg atoms. It leads to an offset in \mathcal{T}_{exp} , best fitted to a typical value 0.2% in \mathcal{T}_{fit} , mapped onto the residual cross section $\sigma_{\text{exp}}/\nu_{\text{ICE}}^3 \sim 10^{-25} \text{ m}^2$ around the AIZs in Fig. 4.

The strong saturation of the observed transfer at the AI resonance, but to a value less than 1, is not compatible with the saturation coefficient $\sigma \Phi T_{\text{ICE}} \sim 50$ (Fig. 4). This effect is attributed to the existence of a small number of Rydberg excitations located out of the main Rydberg cloud, where no ICE light is applied—due, for instance, to speckle in the intensity profiles of the Rydberg-excitation beams. These Rydberg atoms thus survive the ICE pulse without AI, which leads to an apparent decrease of the

maximum value of \mathcal{T}_{exp} . This deviation is represented by a saturation parameter, typically fitted to the best value 0.97 and applied to the fraction of \mathcal{T}_{fit} due to the AI or the extra ion peak signal.

The sharp peak at the ion-core resonance is ascribed to the existence of interactions in the sample. A quantitative description of the induced state dynamics is too involved: here, we confine ourselves to a qualitative discussion. In the presence of a residual electrostatic field, and in particular the field generated by a nearby ion, high- ℓ states can be created over the ICE pulse time scale, arising from the mixing of their multiplicity with the $6sn_g s$ state. At the end of the ICE pulse, atoms remaining in these high- ℓ states participate in the Rydberg signal N_R , undiscriminated from $6sn_g s$ Rydberg atoms. This effect appears to have a negligible influence on the ICE spectra, except around $f_{\text{ICE}} = f_{\text{ion}}$. Indeed, when the AI rate of $6sn_g s$ is high, the dynamics are mainly driven by fast ionization on time scales of nanoseconds or less, completely dominating the state mixing. In regions where the lower-ionization cross sections are observed, very few ions are present and/or created in the sample and moderate state mixing does not perturb the measurement of N_R . On the contrary, around the ionic core resonance, these assumptions fail because high- ℓ states undergo fast AI due to their negligible quantum defects: the field of the ions thereby created accelerates the state mixing, which leads to dynamical self-amplification. As explained above, this narrow peak in the ionization cross section is empirically simulated with an extra cross section σ_L of Lorentzian shape centered on f_{ion} . Best fits yield widths of 1.1 GHz and 700 MHz, respectively, for $n_g=50$ and $n_g = 60$ and a typical maximal amplitude $\sigma_L \sim 10^{-17} \text{ m}^2$. These widths are compatible with high- ℓ states, not with the smaller ICE Rabi frequency applied and not with the (even smaller) ionic core spontaneous rate.

For $n_g = 50$, the situation is different: we observe a significant reduction of σ_{exp} as compared to σ_{MQDT} and an additional pedestal in the cross section close to the ion-core resonance. We attribute these two effects to a strong coincidental resonant interaction, even in the absence of an electric field. Indeed, inspecting the energies of the $6sn_g s \ ^1S_0$ [69] and the $6snp \ ^{1,3}P_1$ [88] Rydberg series, we find that a pair of atoms in $6s50s \ ^1S_0$ state are in Förster resonance [89], within the known uncertainties, with a pair of $6snp \ ^{1,3}P_1$ states, leading to high interactions evaluated between 1 and 10 MHz at our density. We thus interpret the apparent reduction in the ICE cross section as a significant transfer of $6s50s$ Rydberg atoms into $6snp \ ^{1,3}P_1$ states, which autoionize at different ICE laser detunings and also favor increased mixing with high- ℓ states. Additional evidence for this Förster resonance is the pedestal in σ_{exp} , not visible for $n_g = 60$: it is compatible with the AI of the $6snp \ ^{1,3}P_1$ states (see Fig. 4.13 in Ref. [90]). For $n_g = 50$, the best fits yield an amplitude close to $7 \times 10^{-19} \text{ m}^2$ and

a width of 9.5 GHz, both with a few percent uncertainties, whereas for $n_g = 60$, the fitted pedestal is compatible with zero.

4. Cross-section data presentation

We have presented above how spatial variations of the ICE intensity and the Rydberg-cloud density are accounted for and simulated. Starting from the observed transfer \mathcal{T}_{exp} , direct derivation of the AI cross section (i.e., excluding experimental defects) is possible by numerical inversion of the simulation equations with the best-fit results. However, these technical calculations do not yield extra insights into the physics involved in our experiment. Instead, among the best-fit results, we choose to use only w_R , the size of the Rydberg cloud, over which we evaluate the averaged photon flux:

$$\Phi_R = \frac{2P_{\text{ICE}}}{\pi h f_{\text{ion}} (w_{\text{ICE}}^2 + w_R^2)}. \quad (\text{B4})$$

A simplifying hypothesis allowing for a clearer presentation of all the data using cross sections consists in assuming that the Rydberg cloud is illuminated by the uniform ICE photon flux Φ_R . This approximation is acceptable when $w_{\text{ICE}} \gtrsim w_R$, which is the case for the AI-spectra measurements, meaning that AI processes that are strongly nonlinear with the intensity can still be captured with an averaged intensity when it does not vary too much over the Rydberg-cloud extension. More precisely, σ_{exp} is computed following Eq. (1) but after replacement of Φ by Φ_R , \mathcal{T} by \mathcal{T}_{exp} and σ by σ_{exp} . Concerning the simulation results displayed as σ_{fit} , we use a similar approach but we substitute the simulated transfer \mathcal{T}_{fit} and σ_{fit} instead.

APPENDIX C: ANALYSIS OF RYDBERG-EXCITATION SPECTROSCOPY

1. Simulations of the signals

To simulate the signals obtained during Rydberg-excitation spectroscopy, we rely on the analysis of the AI spectra, which yields accurate knowledge of the AI cross section σ . We assume that during the pulse, the Rydberg atoms are created at a rate constant over time, depending on their position within the Rydberg cloud. After their creation, they are possibly autoionized by ICE light with the cross section σ . We also rely on the physical assumptions used to simulate the AI spectra (see Appendix B 2). The Rydberg-excitation light and the ICE light are applied simultaneously, the latter having a calibrated Gaussian intensity profile given by Eq. (B1). At the end of the pulse, we still consider two-dimensional axisymmetric distributions for the surface density of Rydberg atoms $n_R(r)$ (which are created during the pulse and survive until its end without AI), and of ions, denoted by $n_{\text{Ion}}(r)$. A time integration is needed to derive $n_R(r, f_{\text{Ryd}})$ and $n_{\text{Ion}}(r, f_{\text{Ryd}})$

before the surface integration, which yields the overall signals $N_{\text{Ion}}(f_{\text{Ryd}})$ and $N_R(f_{\text{Ryd}})$. In the following, we derive the different formulas concerning increasing physical complexity, starting from the Rydberg excitation in absence of ICE beam (denoted by ‘‘off’’ in Fig. 6), then with the ICE beam at an AIZ (denoted by ‘‘on’’ in Fig. 6), and finally away from an AIZ as presented in Fig. 5.

We first focus on the conditions of Rydberg excitations, considering the so-called reference case when only the Rydberg-excitation beams are applied for a total duration T . Under these conditions, when scanning f_{Ryd} , we thus observe a reference Rydberg signal $N_{\text{ref}}(f_{\text{Ryd}})$ called the excitation profile and no ion signal due to AI: two examples of ‘‘off’’ Rydberg-excitation profiles are given in Fig. 6. We denote by $f_{R,0}$ the resonance condition for the Rydberg excitation, i.e., when $f_{\text{Ryd}} = f_{R,0}$, $N_{\text{ref}}(f_{R,0})$ is maximal. This is precisely the condition of Rydberg-cloud creation before applying ICE light during AI-spectra measurements. Under the previously cited assumptions, if we further denote by $n_{\text{ref}}(r)$ the value of $n_R(r)$ obtained at resonance, its expression is formally identical to Eq. (B2):

$$n_{\text{ref}}(r) = \frac{2N_{\text{ref}}(f_{R,0})}{\pi w_R^2} e^{-2r^2/w_R^2}, \quad (\text{C1})$$

where w_R is the effective waist of the Rydberg cloud introduced in Sec. III C and already used in the simulations of AI spectra. The resonant value of the Rydberg-excitation rate per unit surface γ_R is thus deduced by inverting the time integration, yielding $\gamma_R(r, f_{R,0}) = n_{\text{ref}}(r)/T$. Dedicated studies of various excitation profiles have shown that they are best described by Voigt profiles centered on $f_{R,0}$, obtained as a convolution between a Gaussian profile of width (FWHM) denoted by w_G and a Lorentzian profile of width w_L : this is consistent with an averaging over individual Lorentzian excitation profiles that are shifted by the interactions with other Rydberg atoms in the cloud with a random distribution. We thus consider that $N_{\text{ref}}(f_{\text{Ryd}}) = N_{\text{ref}}(f_{R,0}) \mathcal{V}(f_{\text{Ryd}} - f_{R,0}; w_G, w_L)$, where \mathcal{V} is a centered Voigt profile with unit maximal value. This enables us to deduce the Rydberg-excitation rate per unit surface at position r and at any excitation frequency f :

$$\begin{aligned} \gamma_R(r, f; f_{R,0}) &= \frac{n_{\text{ref}}(r)}{T} \mathcal{V}(f - f_{R,0}) \\ &= \Gamma_R \mathcal{V}(f - f_{R,0}) e^{-2r^2/w_R^2}, \end{aligned}$$

with

$$\Gamma_R = \frac{2N_{\text{ref}}(f_{R,0})}{(\pi w_R^2 T)}, \quad (\text{C2})$$

where the parameters w_G and w_L are implied in \mathcal{V} . Γ_R is the peak Rydberg-excitation rate per unit surface at the

Rydberg-cloud center and represents a scaling parameter on the signals in the simulation along with w_R .

In a second step, we consider that ICE light is applied simultaneously with the excitation pulse (thus $T_{\text{ICE}} = T$) but at an AIZ: ICE light only shifts the Rydberg-excitation resonance frequency and no AI occurs. We denote by $K_S = (\Delta f)_{\text{ICE}}/I$ the ICE spectral shift per unit intensity introduced in Sec. II A, the fundamental quantity we wish to measure in a Rydberg-excitation spectroscopy. The Rydberg-excitation rate per unit surface at position r is thus obtained after shifting the resonance frequency by a quantity $K_S I(r)$, yielding the value $\gamma_R[r, f; f_{R,0} + K_S I(r)]$. Time integration immediately yields the Rydberg-atom surface density $n_R(r) = \gamma_R(r) T$ obtained when no AI occurs, which also corresponds to the total density of Rydberg excitations at position denoted by n_{tot} :

$$\frac{n_{\text{tot}}(r, f_{\text{Ryd}})}{T} = \Gamma_R \mathcal{V}[f_{\text{Ryd}} - f_{R,0} - K_S I(r)] e^{-2r^2/w_R^2}. \quad (\text{C3})$$

The Rydberg signal obtained under these conditions, termed $N_{\text{tot}}(f_{\text{Ryd}})$, is derived after surface integration of $n_{\text{tot}}(r)$: this integration is computed numerically and results in the Rydberg signals denoted by ‘‘on’’ in Fig. 6 (red or blue full lines).

Finally, we consider the case of application of ICE light away from an AIZ. The previously cited surface integration $N_{\text{tot}}(f_{\text{Ryd}})$ is still valid to calculate the total number of Rydberg excitations that occur in the sample $N_R(f_{\text{Ryd}}) + N_{\text{Ion}}(f_{\text{Ryd}})$ but not the number of Rydberg atoms at the end of the pulse, since a fraction of the created Rydberg atoms have undergone AI. To obtain the relative contribution of ions and Rydberg atoms in the signal, one derives $n_R(r)$ by integrating over time t the Rydberg-excitation rate per unit surface [which corresponds to n_{tot}/T given by Eq. (C3)] multiplied by the survival probability $1 - \mathcal{T}$ [Eq. (1)]. Here, the expression for \mathcal{T} uses the local photon flux $\Phi(r) = I(r)/(hf_{\text{ion}})$ and the remaining illumination time $T - t$. One obtains

$$n_R(r, f_{\text{Ryd}}) = \int_0^T dt \frac{n_{\text{tot}}(r, f_{\text{Ryd}})}{T} e^{-\sigma \Phi(r)(T-t)}. \quad (\text{C4})$$

The analytical formula obtained after such time integration is inserted into the surface integration of n_R (also computed numerically), which yields $N_R(f_{\text{Ryd}})$ and $N_{\text{Ion}}(f_{\text{Ryd}}) = N_{\text{tot}}(f_{\text{Ryd}}) - N_R(f_{\text{Ryd}})$. Figure 5 illustrates the signals N_{Ion} and N_R simulated in this way, obtained after the best-fit procedures described below. Note that $N_R \neq N_{\text{tot}}$, meaning that the Rydberg signal is different from the previously termed reference signal (Rydberg-excitation profile obtained without ICE illumination), which is not recorded during the ICE light-shift measurements out of the AIZs. In the comments around Fig. 5, the description of N_R used as

a frequency reference is only qualitative but relates to the fact that this signal dominates in the determination of $f_{R,0}$.

2. Best-fit procedures

The best-fit procedures that yield the ICE spectral shift $K_S = (\Delta f)_{\text{ICE}}/I$ use the simulations described above to find the best match between the simulated and measured signals $N_{\text{Ion}}(f_{\text{Ryd}})$ and $N_R(f_{\text{Ryd}})$.

Physical quantities that are previously known are described by constant input parameters: these are the ICE beam properties P_{ICE} and w_{ICE} , enabling the computation of the intensity distribution with Eq. (B1), the pulse duration $T = T_{\text{ICE}}$, and the AI cross section σ . For $n_g = 60$ and $n_g = 72$, we use the theoretical cross section σ_{MQDT} given by our AI-spectra measurements following Eq. (A3), while for $n_g = 50$, we use $\sigma = 0.34 \times \sigma_{\text{MQDT}}$ as a best guess for the experimentally observed cross section during the light-shift measurements. For each recorded Rydberg-excitation spectrum, we also account for the ion background count observed and evaluate it by averaging the ion signal observed far from any signal due to Rydberg excitation and/or AI.

Five parameters are adjusted during the best-fit procedures: the reference resonant Rydberg creation rate serving as an overall scaling parameter of the signals (formally, the parameter Γ_R in Eq. (C2), but rescaled due to the use of dimensionless units in the numerical integration); the Rydberg-excitation resonant frequency $f_{R,0}$ (close to zero in Figs. 5 and 6 after arbitrary offset subtraction); the Rydberg-cloud effective waist w_R ; the spectral widths w_G and w_L that describe the excitation profile via a Voigt function; and the ICE spectral shift per unit intensity, previously denoted by K_S .

For ICE light-shift measurements performed out of AIZs, the best-fit procedure searches the overall best match between the recorded Rydberg and ion signals and $N_R(f_{\text{Ryd}})$ and $N_{\text{Ion}}(f_{\text{Ryd}})$ as defined following Eqs. (C3) and (C4). For measurements performed at an AIZ, the reference signal (excitation profile) recorded without ICE light is compared with the calculated Voigt function scaled by Γ_R , while the Rydberg signal obtained under ICE illumination is compared with the calculated Rydberg signal $N_{\text{tot}}(f_{\text{Ryd}})$ defined following Eq. (C3).

3. Limitations of the model

The model used to simulate the ion and Rydberg signals uses strong assumptions, among which are a Gaussian shape for the density of the Rydberg cloud (integrated along the ICE propagation axis), an ICE beam perfectly centered on the cloud, and a constant Rydberg-excitation rate without any memory effect with regard to AI. While the two first assumptions appear as a reasonable guess when considering the uncontrolled fluctuations in our experiment, the last assumption deserves inspection.

Indeed, when a Rydberg atom is ionized, we expect a perturbation of the subsequent Rydberg excitations in its vicinity, caused by the Coulomb field created. We thus expect that the constant-Rydberg-excitation-rate hypothesis will fail for conditions with the highest AI rates, which increase the ion density, and with the strongest ICE light shifts, which will spatially restrict the Rydberg-excitation resonance condition inside the focused ICE beam. Experimentally, this failure will be favored by higher n_g numbers (because AI rates and light shifts scale as n_g^3) and an ICE frequency tuning close to the AI resonance (larger AI rates and light shifts): this will be manifested, for measurements exhibiting the larger N_{Ion}/N_R ratio at the peak of the signals (around the excitation resonant frequency $f_{R,0}$), by a failure in the simulations to capture the location of the cutoff in ion signal in the far wing of the peaks (this cutoff is illustrated in Fig. 5). We accordingly decide to discard the associated light-shift measurements when they meet all of the three following criteria: a strong AI cross section $\sigma > 10^{-18} \text{ m}^2$; a strong predicted ICE light shift $[(\Delta f)_{\text{ICE}} > 15 \text{ MHz in the center of the beam}]$; and obvious failure of the simulated ion signal to capture the observed cutoff. Three light-shift measurements out of 16 are discarded following these criteria, all performed with the highest principal quantum number tested, $n_g = 72$, and closest to the AI resonance ($f_{\text{ICE}} - f_{\text{AI}} < 3.7 \text{ GHz}$ yielding $|\Delta v_{\text{ICE}} - (\delta_g - \delta_e)| < 0.16$). Note that the measurement displayed at $\Delta v_{\text{ICE}} \simeq 0.17$ in Fig. 7 meets the first two criteria but obviously not the third (the good accordance between the measured and simulated ion signals is reflected by the low statistical uncertainty displayed): although we conclude that the large mismatch between the calculated and measured light shift is probably due to this limitation, the measurement is not discarded.

[1] T. F. Gallagher, *Rydberg Atoms*, Cambridge Monographs on Atomic, Molecular and Chemical Physics (Cambridge University Press, 1994).

[2] D. Jaksch, J. I. Cirac, P. Zoller, S. L. Rolston, R. Côté, and M. D. Lukin, Fast Quantum Gates for Neutral Atoms, *Phys. Rev. Lett.* **85**, 2208 (2000).

[3] M. D. Lukin, M. Fleischhauer, R. Cote, L. M. Duan, D. Jaksch, J. I. Cirac, and P. Zoller, Dipole Blockade and Quantum Information Processing in Mesoscopic Atomic Ensembles, *Phys. Rev. Lett.* **87**, 037901 (2001).

[4] H. Weimer, M. Müller, I. Lesanovsky, P. Zoller, and H. P. Büchler, A Rydberg quantum simulator, *Nat. Phys.* **6**, 382 (2010).

[5] M. Saffman, T. G. Walker, and K. Mølmer, Quantum information with Rydberg atoms, *Rev. Mod. Phys.* **82**, 2313 (2010).

[6] T. F. Gallagher and P. Pillet, in *Advances in Atomic, Molecular, and Optical Physics*, Vol. 56 (Academic Press, 2008), p. 161.

[7] A. Browaeys, D. Barredo, and T. Lahaye, Experimental investigations of dipole-dipole interactions between a few Rydberg atoms, *J. Phys. B: At., Mol. Opt. Phys.* **49**, 152001 (2016).

[8] P. Schauß, M. Cheneau, M. Endres, T. Fukuhara, S. Hild, A. Omran, T. Pohl, C. Gross, S. Kuhr, and I. Bloch, Observation of spatially ordered structures in a two-dimensional Rydberg gas, *Nature* **491**, 87 (2012).

[9] P. Schauß, J. Zeiher, T. Fukuhara, S. Hild, M. Cheneau, T. Macri, T. Pohl, I. Bloch, and C. Gross, Crystallization in Ising quantum magnets, *Science* **347**, 1455 (2015).

[10] J. Zeiher, R. van Bijnen, P. Schauß, S. Hild, J.-y. Choi, T. Pohl, I. Bloch, and C. Gross, Many-body interferometry of a Rydberg-dressed spin lattice, *Nat. Phys.* **12**, 1095 (2016).

[11] C. Gross and I. Bloch, Quantum simulations with ultracold atoms in optical lattices, *Science* **357**, 995 (2017).

[12] M. Saffman, Quantum computing with atomic qubits and Rydberg interactions: Progress and challenges, *J. Phys. B: At., Mol. Opt. Phys.* **49**, 202001 (2016).

[13] A. Browaeys and T. Lahaye, Many-body physics with individually controlled Rydberg atoms, *Nat. Phys.* **16**, 132 (2020).

[14] L. Henriët, L. Beguin, A. Signoles, T. Lahaye, A. Browaeys, G.-O. Reymond, and C. Jurczak, Quantum computing with neutral atoms, *Quantum* **4**, 327 (2020).

[15] H. Bernien, S. Schwartz, A. Keesling, H. Levine, A. Omran, H. Pichler, S. Choi, A. S. Zibrov, M. Endres, M. Greiner, V. Vuletić, and M. D. Lukin, Probing many-body dynamics on a 51-atom quantum simulator, *Nature* **551**, 579 (2017).

[16] S. de Léséleuc, S. Weber, V. Lienhard, D. Barredo, H. P. Büchler, T. Lahaye, and A. Browaeys, Accurate Mapping of Multilevel Rydberg Atoms on Interacting Spin-1/2 Particles for the Quantum Simulation of Ising Models, *Phys. Rev. Lett.* **120**, 113602 (2018).

[17] A. Keesling, A. Omran, H. Levine, H. Bernien, H. Pichler, S. Choi, R. Samajdar, S. Schwartz, P. Silvi, S. Sachdev, P. Zoller, M. Endres, M. Greiner, V. Vuletić, and M. D. Lukin, Quantum Kibble-Zurek mechanism and critical dynamics on a programmable Rydberg simulator, *Nature* **568**, 207 (2019).

[18] S. de Léséleuc, V. Lienhard, P. Scholl, D. Barredo, S. Weber, N. Lang, H. P. Büchler, T. Lahaye, and A. Browaeys, Observation of a symmetry-protected topological phase of interacting bosons with Rydberg atoms, *Science* **365**, 775 (2019).

[19] M. Schlosser, D. O. de Mello, D. Schäffner, T. Preuschoff, L. Kohfahl, and G. Birkl, Assembled arrays of Rydberg-interacting atoms, *J. Phys. B: At., Mol. Opt. Phys.* **53**, 144001 (2020).

[20] S. Ebadi, T. T. Wang, H. Levine, A. Keesling, G. Semeghini, A. Omran, D. Bluvstein, R. Samajdar, H. Pichler, W. W. Ho, S. Choi, S. Sachdev, M. Greiner, V. Vuletić, and M. D. Lukin, Quantum phases of matter on a 256-atom programmable quantum simulator, *Nature* **595**, 227 (2021).

[21] P. Scholl, M. Schuler, H. J. Williams, A. A. Eberharter, D. Barredo, K.-N. Schymik, V. Lienhard, L.-P. Henry, T. C. Lang, T. Lahaye, A. M. Läuchli, and A. Browaeys, Quantum simulation of 2D antiferromagnets with hundreds of Rydberg atoms, *Nature* **595**, 233 (2021).

- [22] H. Levine, A. Keesling, A. Omran, H. Bernien, S. Schwartz, A. S. Zibrov, M. Endres, M. Greiner, V. Vuletić, and M. D. Lukin, High-Fidelity Control and Entanglement of Rydberg-Atom Qubits, *Phys. Rev. Lett.* **121**, 123603 (2018).
- [23] T. M. Graham, M. Kwon, B. Grinkemeyer, Z. Marra, X. Jiang, M. T. Lichtman, Y. Sun, M. Ebert, and M. Saffman, Rydberg-Mediated Entanglement in a Two-Dimensional Neutral Atom Qubit Array, *Phys. Rev. Lett.* **123**, 230501 (2019).
- [24] H. Levine, A. Keesling, G. Semeghini, A. Omran, T. T. Wang, S. Ebadi, H. Bernien, M. Greiner, V. Vuletić, H. Pichler, and M. D. Lukin, Parallel Implementation of High-Fidelity Multiqubit Gates with Neutral Atoms, *Phys. Rev. Lett.* **123**, 170503 (2019).
- [25] H. Labuhn, S. Ravets, D. Barredo, L. Béguin, F. Nogrette, T. Lahaye, and A. Browaeys, Single-atom addressing in microtraps for quantum-state engineering using Rydberg atoms, *Phys. Rev. A* **90**, 023415 (2014).
- [26] T. Xia, M. Lichtman, K. Maller, A. W. Carr, M. J. Piotrowicz, L. Isenhower, and M. Saffman, Randomized Benchmarking of Single-Qubit Gates in a 2D Array of Neutral-Atom Qubits, *Phys. Rev. Lett.* **114**, 100503 (2015).
- [27] G. Günter, H. Schempp, M. Robert-de Saint-Vincent, V. Gavryusev, S. Helmrich, C. S. Hofmann, S. Whitlock, and M. Weidemüller, Observing the dynamics of dipole-mediated energy transport by interaction-enhanced imaging, *Science* **342**, 954 (2013).
- [28] S. Zhang, F. Robicheaux, and M. Saffman, Magic-wavelength optical traps for Rydberg atoms, *Phys. Rev. A* **84**, 043408 (2011).
- [29] S. de Léséleuc, D. Barredo, V. Lienhard, A. Browaeys, and T. Lahaye, Optical Control of the Resonant Dipole-Dipole Interaction between Rydberg Atoms, *Phys. Rev. Lett.* **119**, 053202 (2017).
- [30] S. K. Dutta, J. R. Guest, D. Feldbaum, A. Walz-Flannigan, and G. Raithel, Ponderomotive Optical Lattice for Rydberg Atoms, *Phys. Rev. Lett.* **85**, 5551 (2000).
- [31] K. C. Younge, B. Knuffman, S. E. Anderson, and G. Raithel, State-Dependent Energy Shifts of Rydberg Atoms in a Ponderomotive Optical Lattice, *Phys. Rev. Lett.* **104**, 173001 (2010).
- [32] S. E. Anderson, K. C. Younge, and G. Raithel, Trapping Rydberg Atoms in an Optical Lattice, *Phys. Rev. Lett.* **107**, 263001 (2011).
- [33] D. Barredo, V. Lienhard, P. Scholl, S. de Léséleuc, T. Boulier, A. Browaeys, and T. Lahaye, Three-Dimensional Trapping of Individual Rydberg Atoms in Ponderomotive Bottle Beam Traps, *Phys. Rev. Lett.* **124**, 023201 (2020).
- [34] R. G. Cortiñas, M. Favier, B. Ravon, P. Méhaignerie, Y. Machu, J. M. Raimond, C. Sayrin, and M. Brune, Laser Trapping of Circular Rydberg Atoms, *Phys. Rev. Lett.* **124**, 123201 (2020).
- [35] S. de Léséleuc, D. Barredo, V. Lienhard, A. Browaeys, and T. Lahaye, Analysis of imperfections in the coherent optical excitation of single atoms to Rydberg states, *Phys. Rev. A* **97**, 053803 (2018).
- [36] F. B. Dunning, T. C. Killian, S. Yoshida, and J. Burgdörfer, Recent advances in Rydberg physics using alkaline-earth atoms, *J. Phys. B: At., Mol. Opt. Phys.* **49**, 112003 (2016).
- [37] A. V. Gorshkov, M. Hermele, V. Gurarie, C. Xu, P. S. Julienne, J. Ye, P. Zoller, E. Demler, M. D. Lukin, and A. M. Rey, Two-orbital $SU(N)$ magnetism with ultracold alkaline-earth atoms, *Nat. Phys.* **6**, 289 (2010).
- [38] F. Gerbier and J. Dalibard, Gauge fields for ultracold atoms in optical superlattices, *New J. Phys.* **12**, 033007 (2010).
- [39] A. J. Daley, M. M. Boyd, J. Ye, and P. Zoller, Quantum Computing with Alkaline-Earth-Metal Atoms, *Phys. Rev. Lett.* **101**, 170504 (2008).
- [40] A. V. Gorshkov, A. M. Rey, A. J. Daley, M. M. Boyd, J. Ye, P. Zoller, and M. D. Lukin, Alkaline-Earth-Metal Atoms as Few-Qubit Quantum Registers, *Phys. Rev. Lett.* **102**, 110503 (2009).
- [41] S. Stellmer, B. Pasquiou, R. Grimm, and F. Schreck, Laser Cooling to Quantum Degeneracy, *Phys. Rev. Lett.* **110**, 263003 (2013).
- [42] R. Yamamoto, J. Kobayashi, T. Kuno, K. Kato, and Y. Takahashi, An ytterbium quantum gas microscope with narrow-line laser cooling, *New J. Phys.* **18**, 023016 (2016).
- [43] M. A. Norcia, A. W. Young, and A. M. Kaufman, Microscopic Control and Detection of Ultracold Strontium in Optical-Tweezer Arrays, *Phys. Rev. X* **8**, 041054 (2018).
- [44] A. Cooper, J. P. Covey, I. S. Madjarov, S. G. Porsev, M. S. Safronova, and M. Endres, Alkaline-Earth Atoms in Optical Tweezers, *Phys. Rev. X* **8**, 041055 (2018).
- [45] S. Saskin, J. T. Wilson, B. Grinkemeyer, and J. D. Thompson, Narrow-Line Cooling and Imaging of Ytterbium Atoms in an Optical Tweezer Array, *Phys. Rev. Lett.* **122**, 143002 (2019).
- [46] J. P. Covey, I. S. Madjarov, A. Cooper, and M. Endres, 2000-Times Repeated Imaging of Strontium Atoms in Clock-Magic Tweezer Arrays, *Phys. Rev. Lett.* **122**, 173201 (2019).
- [47] I. S. Madjarov, J. P. Covey, A. L. Shaw, J. Choi, A. Kale, A. Cooper, H. Pichler, V. Schkolnik, J. R. Williams, and M. Endres, High-fidelity entanglement and detection of alkaline-earth Rydberg atoms, *Nat. Phys.* **16**, 857 (2020).
- [48] R. Mukherjee, J. Millen, R. Nath, M. P. A. Jones, and T. Pohl, Many-body physics with alkaline-earth Rydberg lattices, *J. Phys. B: At., Mol. Opt. Phys.* **44**, 184010 (2011).
- [49] W. E. Cooke, T. F. Gallagher, S. A. Edelstein, and R. M. Hill, Doubly Excited Autoionizing Rydberg States of Sr, *Phys. Rev. Lett.* **40**, 178 (1978).
- [50] J. Millen, G. Lochead, and M. P. A. Jones, Two-Electron Excitation of an Interacting Cold Rydberg Gas, *Phys. Rev. Lett.* **105**, 213004 (2010).
- [51] J. Millen, G. Lochead, G. R. Corbett, R. M. Potvliege, and M. P. A. Jones, Spectroscopy of a cold strontium Rydberg gas, *J. Phys. B: At., Mol. Opt. Phys.* **44**, 184001 (2011).
- [52] P. McQuillen, X. Zhang, T. Strickler, F. B. Dunning, and T. C. Killian, Imaging the evolution of an ultracold strontium Rydberg gas, *Phys. Rev. A* **87**, 013407 (2013).
- [53] G. Lochead, D. Boddy, D. P. Sadler, C. S. Adams, and M. P. A. Jones, Number-resolved imaging of excited-state atoms using a scanning autoionization microscope, *Phys. Rev. A* **87**, 053409 (2013).
- [54] J. T. Wilson, S. Saskin, Y. Meng, S. Ma, R. Dilip, A. P. Burgers, and J. D. Thompson, Trapping Alkaline Earth Rydberg Atoms Optical Tweezer Arrays, *Phys. Rev. Lett.* **128**, 033201 (2022).
- [55] R. R. Jones and T. F. Gallagher, Autoionization of high- l Ba $6p_{1/2}nl$ states, *Phys. Rev. A* **38**, 2846 (1988).
- [56] R. R. Jones, C. J. Dai, and T. F. Gallagher, Ba $6p_jnf_j'$ autoionizing series, *Phys. Rev. A* **41**, 316 (1990).

- [57] H. Lehec, X. Hua, P. Pillet, and P. Cheinet, Isolated core excitation of high-orbital-quantum-number Rydberg states of ytterbium, *Phys. Rev. A* **103**, 022806 (2021).
- [58] R. C. Teixeira, A. Larrouy, A. Muni, L. Lachaud, J.-M. Raimond, S. Gleyzes, and M. Brune, Preparation of Long-Lived, Non-Autoionizing Circular Rydberg States of Strontium, *Phys. Rev. Lett.* **125**, 263001 (2020).
- [59] K. A. Safinya and T. F. Gallagher, Observation of Interferences between Discrete Autoionizing States in the Photoexcitation Spectrum of Barium, *Phys. Rev. Lett.* **43**, 1239 (1979).
- [60] N. H. Tran, R. Kachru, and T. F. Gallagher, Multistep laser excitation of barium: Apparent interferences due to overlap-integral variations, *Phys. Rev. A* **26**, 3016 (1982).
- [61] A. P. Burgers, S. Ma, S. Saskin, J. Wilson, M. A. Alarcón, C. H. Greene, and J. D. Thompson, Controlling Rydberg Excitations Using Ion-Core Transitions in Alkaline-Earth Atom-Tweezer Arrays, *PRX Quantum* **3**, 020326 (2022).
- [62] M. J. Seaton, Quantum defect theory, *Rep. Prog. Phys.* **46**, 167 (1983).
- [63] S. A. Bhatti and W. E. Cooke, Power-dependent line shapes of transitions to autoionizing Rydberg states, *Phys. Rev. A* **28**, 756 (1983).
- [64] W. E. Cooke and C. L. Cromer, Multichannel quantum-defect theory and an equivalent N-level system, *Phys. Rev. A* **32**, 2725 (1985).
- [65] U. Fano, Effects of configuration interaction on intensities and phase shifts, *Phys. Rev.* **124**, 1866 (1961).
- [66] C. Cohen-Tannoudji, G. Grynberg, and J. Dupont-Roc, *Atom-Photon Interactions: Basic Processes and Applications* (Wiley, New York, 1992).
- [67] R. M. Jopson, R. R. Freeman, W. E. Cooke, and J. Bokor, Electron Shake-Up in Two-Photon Excitation of Core Electrons to Rydberg Autoionizing States, *Phys. Rev. Lett.* **51**, 1640 (1983).
- [68] S. A. Bhatti, C. L. Cromer, and W. E. Cooke, Analysis of the Rydberg character of the $5d7d^1D_2$ state of barium, *Phys. Rev. A* **24**, 161 (1981).
- [69] H. Lehec, A. Zuliani, W. Mainault, E. Luc-Koenig, P. Pillet, P. Cheinet, F. Niyaz, and T. F. Gallagher, Laser and microwave spectroscopy of even-parity Rydberg states of neutral ytterbium and multichannel-quantum-defect-theory analysis, *Phys. Rev. A* **98**, 062506 (2018).
- [70] I. Zalivako, I. Semerikov, A. Borisenko, V. Smirnov, P. Vishnyakov, M. Aksenov, P. Sidorov, N. Kolachevsky, and K. Khabarova, Improved wavelength measurement of $2S_{1/2} \rightarrow 2P_{1/2}$ and $2D_{3/2} \rightarrow 3[3/2]_{1/2}$ transitions in Yb^+ , *J. Russ. Laser Res.* **40**, 375 (2019).
- [71] E. H. Pinnington, G. Rieger, and J. A. Kernahan, Beam-laser measurements of the lifetimes of the $6p$ levels in Yb II, *Phys. Rev. A* **56**, 2421 (1997).
- [72] I. Mourachko, D. Comparat, F. de Tomasi, A. Fioretti, P. Nosbaum, V. M. Akulin, and P. Pillet, Many-Body Effects in a Frozen Rydberg Gas, *Phys. Rev. Lett.* **80**, 253 (1998).
- [73] W. E. Cooke and T. F. Gallagher, Observation of Pair Splittings in the Autoionization Spectrum of Ba, *Phys. Rev. Lett.* **41**, 1648 (1978).
- [74] E. Y. Xu, Y. Zhu, O. C. Mullins, and T. F. Gallagher, Sr $5p_{1/2} ns_{1/2}$ and $5p_{3/2} ns_{1/2} J = 1$ autoionizing states, *Phys. Rev. A* **33**, 2401 (1986).
- [75] T. F. Gallagher, R. Kachru, N. H. Tran, and H. B. van Linden van den Heuvell, Two-Photon Excitation of Autoionizing States through Zeros in the Continuum, *Phys. Rev. Lett.* **51**, 1753 (1983).
- [76] U. Fano, G. Pupillo, A. Zannoni, and C. W. Clark, On the absorption spectrum of noble gases at the arc spectrum limit, *J. Res. Natl. Inst. Stand. Technol.* **110**, 583 (2005).
- [77] M. Génévriez, D. Wehrli, and F. Merkt, Experimental and theoretical study of core-excited $3pnd$ Rydberg series of Mg, *Phys. Rev. A* **100**, 032517 (2019).
- [78] A. Jenkins, J. W. Lis, A. Senoo, W. F. McGrew, and A. M. Kaufman, Ytterbium nuclear-spin qubits in an optical tweezer array (2021), [ArXiv:2112.06732](https://arxiv.org/abs/2112.06732).
- [79] L. Pruvost, P. Camus, J.-M. Lecomte, C. Mahon, and P. Pillet, High angular momentum $6pnl$ and $6dnl$ doubly excited Rydberg states of barium, *J. Phys. B: At., Mol. Opt. Phys.* **24**, 4723 (1991).
- [80] P. Camus, P. Pillet, and J. Boulmer, Spectroscopic studies of $9dn'd$ doubly excited autoionising states of neutral barium, *J. Phys. B: At., Mol. Opt. Phys.* **18**, L481 (1985).
- [81] P. Camus, T. F. Gallagher, J.-M. Lecomte, P. Pillet, L. Pruvost, and J. Boulmer, Observation of an Electronic Correlation for Double-Rydberg States of Barium, *Phys. Rev. Lett.* **62**, 2365 (1989).
- [82] U. Eichmann, V. Lange, and W. Sandner, Positional Correlation in Laser-Excited Three-Body Coulomb Systems, *Phys. Rev. Lett.* **64**, 274 (1990).
- [83] R. R. Jones and T. F. Gallagher, Experimental observation of angular correlation between Rydberg electrons in the $\text{Ba } n'l'nl$ autoionizing series, *Phys. Rev. A* **42**, 2655 (1990).
- [84] P. Camus, J.-M. Lecomte, C. R. Mahon, P. Pillet, and L. Pruvost, High l double-Rydberg states $7d\{5/2\}nl$ of barium, *J. Phys. II Fr.* **2**, 715 (1992).
- [85] D. D. Yavuz, P. B. Kulatunga, E. Urban, T. A. Johnson, N. Proite, T. Henage, T. G. Walker, and M. Saffman, Fast Ground State Manipulation of Neutral Atoms in Microscopic Optical Traps, *Phys. Rev. Lett.* **96**, 063001 (2006).
- [86] Y. Wang, X. Zhang, T. A. Corcovilos, A. Kumar, and D. S. Weiss, Coherent Addressing of Individual Neutral Atoms in a 3D Optical Lattice, *Phys. Rev. Lett.* **115**, 043003 (2015).
- [87] Y. Wang, A. Kumar, T.-Y. Wu, and D. S. Weiss, Single-qubit gates based on targeted phase shifts in a 3D neutral atom array, *Science* **352**, 1562 (2016).
- [88] M. Aymar, R. J. Champeau, C. Delsart, and O. Robaux, Three-step laser spectroscopy and multichannel quantum defect analysis of odd-parity Rydberg states of neutral ytterbium, *J. Phys. B: At., Mol. Opt. Phys.* **17**, 3645 (1984).
- [89] K. A. Safinya, J. F. Delpéch, F. Gounand, W. Sandner, and T. F. Gallagher, Resonant Rydberg-Atom-Rydberg-Atom Collisions, *Phys. Rev. Lett.* **47**, 405 (1981).
- [90] H. Lehec, *Spectroscopie Rydberg et excitation du coeur isolé d'atomes d'ytterbium ultra-froids*, Thesis, Université Paris-Saclay (2017), <https://tel.archives-ouvertes.fr/tel-01698466/document>.